Effects of ball milling on the structure of cotton cellulose

Zhe Ling · Tuo Wang · Mohamadamin Makarem · Michael Santiago Cintrón · H. N. Cheng · Xue Kang · Markus Bacher · Antje Potthast · Thomas Rosenau, Holly King · Christopher D. Delhom · Sunghyun Nam · J. Vincent Edwards · Seong H. Kim ·, Feng Xu · Alfred D. French*

Zhe Ling · Feng Xu, Beijing Key Laboratory of Lignocellulosic Chemistry, Beijing Forestry University, Beijing 100083, PR China

Zhe Ling · Michael Santiago Cintrón · H. N. Cheng · Holly King · Christopher D. Delhom · Sunghyun Nam · J. Vincent Edwards · Alfred D. French* · Southern Regional Research Center, Agricultural Research Service, USDA, 1100 Robert E. Lee Blvd., New Orleans, LA 70124, USA

Xue Kang, Tuo Wang Department of Chemistry, Louisiana State University, Baton Rouge, LA 70803, USA

Mohamadamin Makarem · Seong H. Kim Department of Chemical Engineering and Material Research Institute, The Pennsylvania State University, University Park, PA 16802, USA

Thomas Rosenau, Markus Bacher, Antje Potthast Department of Chemistry, Division of Chemistry of Renewable Resources, University of Natural Resources and Life Sciences, Konrad-Lorenz-Str. 24, A-3430 Tulln, Austria

Corresponding author:

Alfred D. French

Email: al.french@ars.usda.gov, Tel: 1-5042864410

ORCID: 0000-0002-6220-6448

Prepared for Cellulose 25th Anniversary Special Issue
Version of 10/13/2018

Abstract Cellulose is often described as a mixture of crystalline and amorphous material. A large part of the general understanding of the chemical, biochemical and physical properties of cellulosic materials is thought to depend on the consequences of the ratio of these components. For example, amorphous materials are said to be more reactive and have less tensile strength but comprehensive understanding and definitive analysis remain elusive. Ball milling has been used for decades to increase the ratio of amorphous material. The present work used 13 techniques to follow the changes in cotton fibers (nearly pure cellulose) after ball milling for 15, 45 and 120 minutes. X-ray diffraction results were analyzed with the Rietveld method; DNP (Dynamic Nuclear Polarization) natural abundance 2-D NMR studies in the following paper assisted with the interpretation of the 1-D analyses in the present work. A conventional NMR model's paracrystalline and inaccessible crystallite surfaces were not needed in the model used for the DNP studies. Sum Frequency Generation spectroscopy also showed profound changes as the cellulose was decrystallized. Optical microscopy and FE-SEM results showed the changes in particle size; molecular weight and carbonyl group analyses by gel permeation chromatography (GPC) confirmed chemical changes. Specific surface areas and pore sizes increased. Fourier Transform IR and Raman spectroscopy also indicated progressive changes; some proposed indicators of crystallinity for FTIR were not in good agreement with our results. Thermogravimetric analysis results indicated progressive increase in initial moisture content and some loss in stability.

Keywords Amorphous cellulose · Ball milling · Cellulose Degradation · Crystal structure · Rietveld refinement

Introduction

Cellulose is often described as a two-phase material, with both crystalline and amorphous domains. It is widely thought that crystalline materials are stronger and less-reactive than their amorphous counterparts. Therefore, it has been of interest for nearly a century to understand these two components to better develop structure-function relationships for both natural and modified cellulosic materials.

The idea that cellulose has a crystalline component came from X-ray diffraction. According to the International Union of Crystallographers, any material (including cotton cellulose) that yields a diffraction pattern with sharp peaks is crystalline. Nishiyama et al. (2003a, 2002) published crystal structures of the Iα and Iβ native celluloses from the alga *Cladophora* and tunicate with atomic coordinates, based on both neutron and synchrotron X-ray studies.

The idea that everyday plant cellulose is not entirely crystalline came from several directions. In the case of diffraction, the peaks are not as sharp as those from many smaller molecules. That increase in peak breadth could come from small crystallite size, from defects within the crystal lattice, or from material that lacks organization, causing the crystalline peaks to be more diffuse (Wertz et al. 2010). Concepts of synthetic petrochemical polymers gave us the “fringed micelle” model and its nuanced “fringed fibril” variant (Hearle 1958) that has individual, long molecules passing through numerous domains of local organization. In between these local domains, or crystallites, the molecules lacked sufficient organization to diffract X-rays into sharp peaks. Another insight from diffraction is that the amorphous regions in ramie cellulose are quite small (Nishiyama et al. 2003b) and distances between the regions are comparable to molecular lengths from Leveling Off Degree of Polymerization (LODP) studies.

Isogai and Atalla (1991) regenerated samples by precipitating cellulose from SO_2-diethylamine-dimethylsulfoxide solutions with various precipitants. Unlike other regenerated celluloses, their precipitates were amorphous, and the exact X-ray scattering patterns differed, depending on the particular precipitating anti-solvent. Vibrational spectroscopists identified a group of low frequency vibrations that were necessary conditions for crystallinity (Agarwal et al. 2016). Those vibrations were absent in some native cellulose samples that still give diffraction patterns that the authors interpreted as indications of an aligned but non-crystalline state. These observations indicate that there are nuances to non-crystalline states and models for the disordered components must incorporate flexibility.

Cotton fibers are individual plant cells, and their cell walls, which consist mostly of cellulose, have additional structural features of interest. In particular, the crystallites of native cellulose are composed of molecules with their reducing groups at one end of the crystal, described as parallel packing. Since the crystallites are generally aligned with the fiber axis[1] one might describe the crystallite as oriented with the reducing end of the crystal towards the growth tip of the cotton fiber. Based in part on findings that the molecules in crystals of mercerized cellulose II are packed antiparallel, however, it has been concluded that adjacent to the crystallites "pointed" towards the fiber growth tip, there is another set of cotton crystallites oriented in the opposite direction. This finding was supported by sum frequency generation (SFG) spectroscopic studies (Lee et al. 2014). These oppositely oriented crystallites, each with parallel-packed molecules, can, after swelling with NaOH, merge to create crystals with their molecules packed antiparallel while retaining the overall fiber structure (Sarko et al. 1987; Shibazaki et al. 1997; French et al., 2018).

An early experiment with ball milling reduced the cotton sample to the amorphous state in 30 min (our ball milling system is slower) (Forziati et al. 1950). Subsequently, Segal et al. (1959) developed a crystallinity index (Fig. 1) to

---

[1] Even though cotton has a high microfibril angle (French and Kim 2018) or range of deviations of alignment of microfibrils to the fiber axis, for this discussion the alignment of adjacent microfibrils can be considered to be antiparallel.

indicate the fraction of crystalline material in the sample. That publication has been cited some 3,650 times at this writing, and their equation is often used without proper credit.[2] In that paper, the Segal crystallinity index (CrI) was compared with acid crystallinity, LODP, density, moisture regain, and an infrared crystallinity

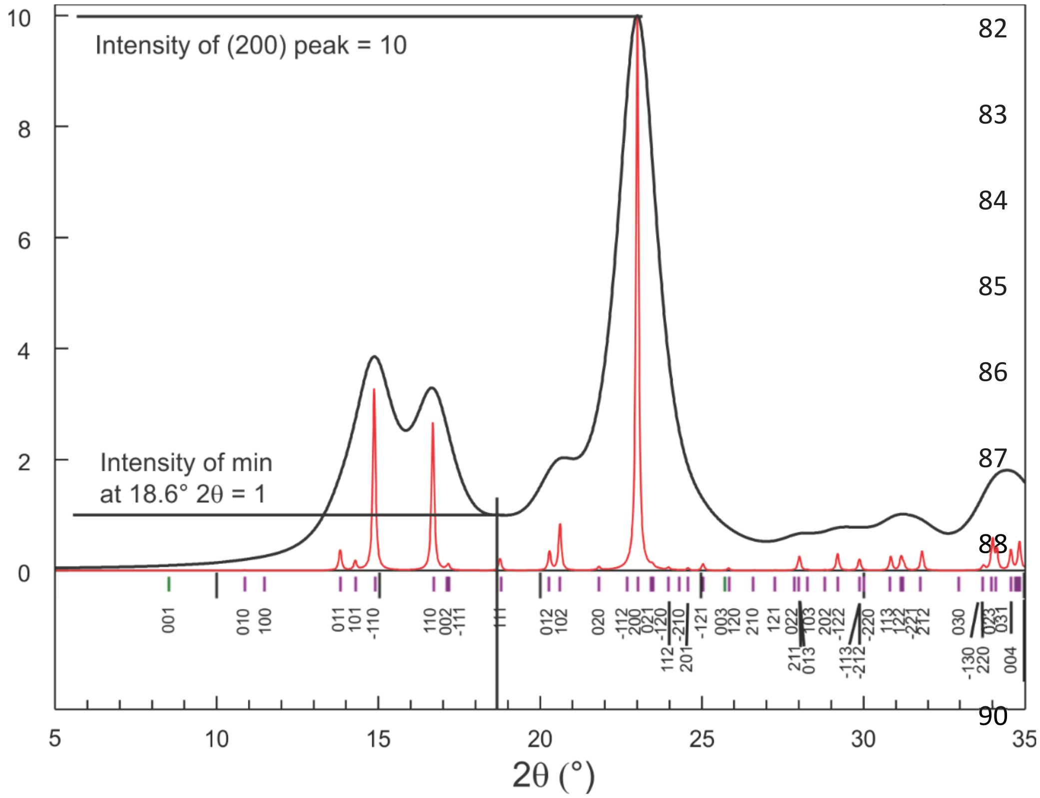

Fig. 1 Calculated diffraction patterns for peak widths at half height (pwhm) of 0.1 (red) and 1.5° (black), based on the crystal structure of cellulose Iβ (Nishiyama et al. 2002). The corresponding Miller indices are plotted for each possible peak,

---

[2] Despite its simplicity, the Segal method is sometimes used incorrectly. The Segal CrI depends on the intensity minimum between the (110) and (200) peaks, as well as the peak intensity of the (200) reflection. However, authors have too-often chosen the (110) or combined (1-10) and (110) peak as representing the amorphous material. Furthermore, for material to be represented by the minimum intensity near 18 deg. (copper Kα radiation), the background must be subtracted. Typically, this would mean subtraction of a blank.

indicated by the vertical magenta lines. The values of 2θ are for a wavelength of 1.5419 Å (CuKα). The Segal CrI is CrI = 100 * $(I_{200} - I_{am})/I_{200}$, where I_{200} is the height of the (200) peak, and I_{am} is the intensity at the minimum at about 18.6° 2θ. Both calculations are based on perfect crystal models, but with sizes of about 900 Å (when pwhm = 0.1°) and 60 Å (pwhm = 1.5°). In this case the smaller crystallite would have a CrI of 90 %, whereas the larger one would have a CrI of 100%. Adapted from Fig. 2a in French (2014)

index. In the intervening years, researchers have attempted to confirm the Segal equation with numerous methods including infrared spectroscopy (Nelson and O'Connor 1964a) and deuterium exchange (Agarwal 2016).

Many such tests could confuse the increase of specific surface area with a decrease in the crystallinity, even though the smaller crystals with more surface area might be perfectly ordered. Another point is that surface molecules become an increasingly large fraction of the total molecules as the crystals are reduced in size. A crystal with 100 molecules (a more or less square shape with 10 molecules on each side) will have 36 molecules (36%) on the surface that are not as constrained by neighbors within the crystal. A similarly shaped crystal with only 36 molecules would have 20 molecules on the surface, or 55%. The O-6 groups on surface molecules would have extra freedom for rotation and occupation of the alternative *gauche-trans* (*gt*) and *gauche-gauche* (*gg*) positions. The O-6 positions will affect various key spectroscopic results more than they would X-ray diffraction intensities. An O-6 in the *gt* position has very similar x- and y- coordinates as one in the usual *trans-gauche* (*tg*) cellulose I position and the very strong hk0 diffraction intensities would not be affected very much. Because different crystallinity techniques measure different things, complete agreement among different methods may never be attained.

Segal's landmark equation was criticized, especially because the area under the peaks is more important than their height. More recently, French and Santiago Cintrón (2013) showed that some of the diffraction intensity attributed to amorphous material by Segal et al. can be due to the overlap of the broad peaks resulting from small crystallites, as in Fig. 1. Also, there is a small contribution to Segal's amorphous intensity from some small peaks. Therefore, no cellulose sample with reasonable crystallite size could give 100 % Segal crystallinity. A further deficit in Segal's approach is that a sample that was 100% amorphous would have to give a diffraction pattern with a flat top. Instead, amorphous samples, regardless of source, give a broad hump with a maximum that reflects the distribution of frequent interatomic distances in the sample.

Park et al. (2010) describe two other methods for crystallinity determination by diffraction: amorphous subtraction and peak deconvolution. The amorphous subtraction method, as in the case of Segal's peak height method, depends on the assumption that the diffraction intensity at the valley between the (110) and (200) peaks is all due to amorphous material, and is thus inherently flawed. The XRD deconvolution method has better fundamentals. However, its implementations suffer because it is typically carried out with curve-fitting software, instead of software written to take into account the specific problems of diffraction data such as preferred orientation and anisotropic crystallite size that are endemic to cellulose samples. Also, only a few strong peaks are usually considered, along with a broad curve that defines the amorphous contribution to the overall intensity. Thus, none of the conventional methods for crystallinity study by diffraction is satisfactory.

In the present work, the Rietveld powder diffraction method is used (Rietveld 1969; Young 1993). This method would seem to be the ultimate approach for diffraction study of cellulose crystallinity and has been applied by a number of researchers including Thygesen et al. (2005), Driemeier and Calligaris (2011), Driemeier (2014), Howell et al. (2011), Chen et al. (2015), Xiaohui et al. (2015), Reyes et al. (2016), Ahvenainen et al. (2016), Duchemin (2017) and Vanderfleet et al. (2018). As also shown in Fig. 1 with the simpler Mercury program, the Rietveld method allows calculation of a theoretical diffraction pattern based on the atomic coordinates of a proposed structure, such as the work of Nishiyama et al. (2002). The question is: what changes to that ideal pattern are needed to make it agree with the observed experimental result? Changes to compensate for variables such as crystallite size, small deviations in unit cell dimensions, and given a model, the presence of amorphous or other phases are optimized with a least squares fit. Even though Rietveld may be the ultimate approach, it is limited by the relatively small amount of data furnished by crystalline cellulose powders, and the X-ray patterns of progressively amorphous material give less and less information.

Nuclear magnetic resonance spectroscopy also has a strong role in cellulose crystallinity studies. Solid-state NMR spectroscopy (ssNMR) has been extensively employed to determine the polymorphic structure of native, functionalized and genetically engineered cellulose (Atalla and Vanderhart 1984; Harris et al. 2012; Wang and Hong 2016; Wickholm et al. 1998). Cellulose crystallinity can be inferred from the intensity ratio of the area under C-4 peaks arising from the crystalline chains that resonate at 87-90 ppm and the area of the disordered domain that shows broader signals spanning 80-86 ppm (Atalla et al. 1980; Newman and Hemmingson 1990; Larsson et al. 1999). This peak broadening is primarily caused by distinct hydroxymethyl torsion angles of C-6: the disordered regions adopt either *gt* or *gg* conformations while the tightly hydrogen-bonded crystallites of cellulose I adopt the *tg* conformation, a structure that is less energetically favored and rarely observed in other carbohydrates (Phyo et al. 2018; Viëtor et al. 2002;

Yang et al. 2018). Further peak complexity exists within each category due to conformational polymorphism, magnetic non-equivalence of glucose units, diverse patterns of chain packing, bundling of multiple microfibrils, and interactions with matrix polymers (Kono and Numata 2006; Newman et al. 2013; Wang et al. 2016). Despite investigation using ssNMR of these complicated structural aspects, an original issue remains and is discussed here. Namely, what is the level of agreement with other spectroscopic or diffraction methods in estimating cellulose crystallinity? Our analyses have been informed by the results given in the accompanying paper (Kirui et al., 2019). In the Supporting Information, an analysis of similar NMR data has been carried out with a more conventional approach in which a model is assumed and the samples were swollen in water prior to measurement.

Of course, many other techniques have been applied to studies of cellulose crystallinity, or at least their results have been interpreted based on changes in crystallinity. As mentioned already, FTIR has been frequently employed (Liu and Kim 2015) as has Raman spectroscopy (Agarwal et al. 2016). Application of SFG spectroscopy specifically to ball-milled cellulose is new. Other techniques are used herein to provide a fuller understanding of the effects of ball milling, including microscopy, molecular weight and oxidation to carbonyl groups determined by multidetector GPC after group-selective fluorescence labeling, surface area and pore size, as well as thermogravimetric analysis. The end of the Results and discussion and the Conclusions sections tie these approaches together.

Experimental

Materials

Cotton balls were purchased from Wal-Mart and chopped in a Wiley mill (Eberbach E3300 mini cutting mill, Eberbach Corp., Belleville, Michigan) until they fell through a 20-mesh screen. Then 5 g portions of the powder were placed in a locally built ball mill (Forziati et al. 1950) running at 1750 rpm. The approximately one liter steel jar was chromium plated and 500 mL of stainless steel balls 0.25 in. (~4 cm) in diameter were employed. The cellulose samples milled for 15 min, 45 min and 120 min were respectively labeled as BMC-15, BMC-45 and BMC-120. The control, Wiley milled cellulose, was denoted as WMC.

Lithium chloride was purchased from JT Baker (Philipsburg, NJ, USA) and ethanol, acetone, and dimethylacetamide (DMAc) were purchased from Sigma Aldrich (St. Louis, MS, USA). All chemicals used in this study were either analytical or reagent grade.

Microscopy

Optical images were obtained with a Zeiss Axioplan polarized light microscope (Thornwood, NY, USA) with an AmScope digital camera (Irvine, CA, USA). Both WMC and BMC samples were dispersed with a pointed tool. The fiber lengths were determined with Image J software (1.41v, US National Institutes of Health, USA).

The samples were also observed with an FEI Quanta 3D FEG Field emission scanning electron microscope (FE-SEM, Hillsboro, Oregon, USA). The accelerating potential was 5 kV, with a beam current of 20 mA. The samples were sputter coated with a 3-nm layer of gold–palladium using a Leica EM ACE600 (Buffalo Grove IL, USA).

Molecular weight determination and carbonyl group analysis

The samples were treated according to a standard protocol (Röhrling et al. 2002) for cellulose labelling (7 days in a shaking water bath at 40°C). After solvent exchange from water to ethanol into DMAc the samples stayed 12 h in DMAc, were dissolved in DMAc/LiCl 9% and diluted with DMAc prior to injection. The raw data are available upon request. The degree of polymerization was calculated by the following equation:

$$DP = M/162 \qquad (1)$$

where M is the molecular weight of each sample and 162 is the molecular weight of an anhydroglucose unit. The maximum molecular lengths (N) were obtained by:

$$N\ (\mathrm{nm}) = DP*0.5125 \qquad (2)$$

where 0.5125 is our estimated advance per glucose residue along an extended but non-symmetric molecule.

Surface properties and thermal analysis

The specific surface area (SSA) and pore sizes of the ball-milled cotton cellulose were measured using Brunauer, Emmet and Teller nitrogen adsorption (Brunauer et al. 1938; Sehaqui et al. 2011) using a TriStar II Plus 2.02 Analyzer (Service purchased from Particle Testing Authority, Norcross, GA, USA). Prior to analysis, samples were under vacuum at 150 °C.

For thermogravimetric (TGA) and differential thermogravimetric (DTG) analyses, all cellulose samples (5 mg each) were conditioned in a Nor-Lake Scientific humidity chamber at 60 °C overnight (Hudson, WI, USA). Tests used a TA Q500 thermogravimetric analyzer (TA Instruments, New Castle, DE) and a nitrogen atmosphere. Samples were heated from 0–600 °C at a rate of 10 °C/min. Thermograms were analyzed by the Universal Analysis 2000 Software (TA Instruments).

Spectroscopy

FTIR spectra were collected on a Vertex 70 (Bruker Optics, Billerica, MA) equipped with a mid-IR source and an attenuated total reflection (ATR) sampling accessory (Pike Technologies, Madison, WI) with a diamond-ZnSe crystal. Samples were placed on top of the ATR crystal and secured with a metal clamp in a manner that assured consistent pressure for all samples. Three measurements were performed for each sample, with a total of 128 scans taken for each sample at a resolution of 4 cm^{-1} (3800 – 600 cm^{-1}). Spectra were corrected against an air background. Spectra for each sample were averaged, baseline-corrected and normalized using the OPUS spectroscopy software (version 6.5). Spectra are presented without ATR correction or atmospheric compensation.

The FT-Raman spectra were collected using a DXR2 785 nm Raman microscope (Thermo Fisher Scientific Inc., USA). The spectra (100-3100 cm^{-1}) were obtained with a laser power of 10 mW, exposure time 1 s with a 25 μm pinhole aperture. Each spectrum was measured once with an accumulation time of 10 s. Spectra were collected by OMNIC for Dispersive Raman software (Thermo Fisher Scientific).

For vibrational SFG spectroscopy, the samples were pressed into pellets. Details of the SFG system have been discussed extensively elsewhere (Lee et al. 2015a). Briefly, SFG beams were generated by spatial and temporal overlap of

800-nm and IR laser beams. A Ti-sapphire amplifier (Coherent, Libra) generated 800-nm laser pulses that were then narrowed by using two Fabry-Pérot etalons to 0.78 nm width. A broadband-tunable IR beam (1000 – 4000 cm^{-1}) with full width at half maximum (FWHM) of 150-200 cm^{-1} is generated using an optical parametric generation/amplification (OPG/OPA) system (Coherent, OPerA Solo). The analysis was carried out with p-polarized IR and s-polarized 800 nm, and the s-polarized SFG signal was recorded. The experiment was done with reflection geometry with two laser beams (IR and 800 nm) shining on samples with a 45° angle. The generated SFG beam was passed through a monochromator and detected by a CCD camera. To minimize the heterogeneity in samples, the spectra were collected from ten randomly chosen locations on the pellets and averaged. Each spectrum was normalized by the IR power.

Solid-state NMR experiments

For the conventional solid-state NMR experiments, 50-59 mg of the native and ball-milled cotton samples were directly packed into 4-mm zirconium rotors for measurements. Solid-state experiments were conducted on a 400 MHz (9.4 Tesla) Bruker Avance spectrometer (Bruker Optics, Billerica MA, USA) using a 4-mm MAS HCN probe. The standard ^{13}C CP experiments were collected under 10 kHz magic-angle spinning (MAS) at 296 K. ^{13}C chemical shifts were externally referenced to adamantane CH_2 signal at 38.48 ppm on the TMS (tetramethylsilane) scale. Typical radiofrequency field strengths were 80 kHz for ^1H decoupling and hard pulse, 62.5 kHz for 1H and ^{13}C CP. A contact time of 1 ms is used for CP. For signal averaging, 12288 scans were measured on each sample. The spectra were deconvoluted using DMfit software (Massiot et al. 2002). The WMC and BMC samples were also processed using a matrix-free protocol for DNP experiments (Takahashi et al. 2012) and the results are detailed in an accompanying separate paper (Kirui et al. 2019).

Diffraction experiments

Laboratory XRD measurements were performed at room temperature with a PANalytical Empyrean laboratory diffractometer (Malvern Panalytical Inc., Westborough MA, USA) with a spinning, zero-background sample holder, using Cu Kα-radiation and a PIXcel3D detector. The patterns were corrected by a blank and then analyzed using the pseudo-Voigt peak shape with the MAUD Rietveld program (Materials Analysis Using Diffraction, version 2.7, Lutterotti et al. 2007). The crystallinity was calculated from the area of the calculated pattern for crystalline cellulose divided by the sum of the areas for crystalline and amorphous regions. The *d*-spacings were calculated from refined unit cell dimensions, and crystallite sizes perpendicular to different lattice planes were calculated using the Scherrer Equation (3).

$$L_{hkl} = \frac{0.9\lambda}{B_{hkl}\, cos\,\theta} \qquad (3)$$

where λ is the X-ray wavelength, B_{hkl} is the angular FWHM in radians of the (hkl) line profile, and θ is the scattering angle (Holzwarth and Gibson 2011).

Synchrotron measurements were performed at beamline 6B of the Center for Advanced Microstructures and Devices (CAMD) (Baton Rouge, Louisiana, USA). Samples of 1 mg of milled cotton were placed in a plastic capillary (MiTeGen MicroRT, Ithaca NY) for which the background scattering pattern was individually recorded immediately prior to filling and collecting the data. Exposure time was 10 s and wavelength λ=1.38 Å. The MAR 2048 x 2048 CCD detector synchrotron data were visualized and converted to 1D data with the XRD2D Scan software (Rodriguez-Navarro 2006). The Caglioti asymmetry parameters in the MAUD Rietveld program were adjusted from their Bragg-Brentano defaults (used with the laboratory data) to zero, and the HWHM Caglioti value0 was set to 0.00025; the value1 and value2 parameters were set to 0.

For visual comparison (Figs. 9 and 10), the synchrotron X-ray patterns (λ=1.3801Å) were converted to the same 2θ scale as the laboratory data (λ=1.5418 Å) by solving the Bragg equation (4) (Klug and Alexander 1974) for *d*

$$n\lambda = 2d\sin\theta \qquad (4)$$

and then converting the *d* value to 2θ with the Bragg equation’s arcsin inverse.

Results and discussion

Optical microscopy and FE-SEM

Polarized light optical micrographs of the samples are in Fig. S1. Previously immersed and dispersed in alcohol, many particles in the WMC and BMC-15 samples were birefringent under polarized light. WMC showed intact and long cellulose fibers with an average length of 296 μm. Ball milling for 15 min broke

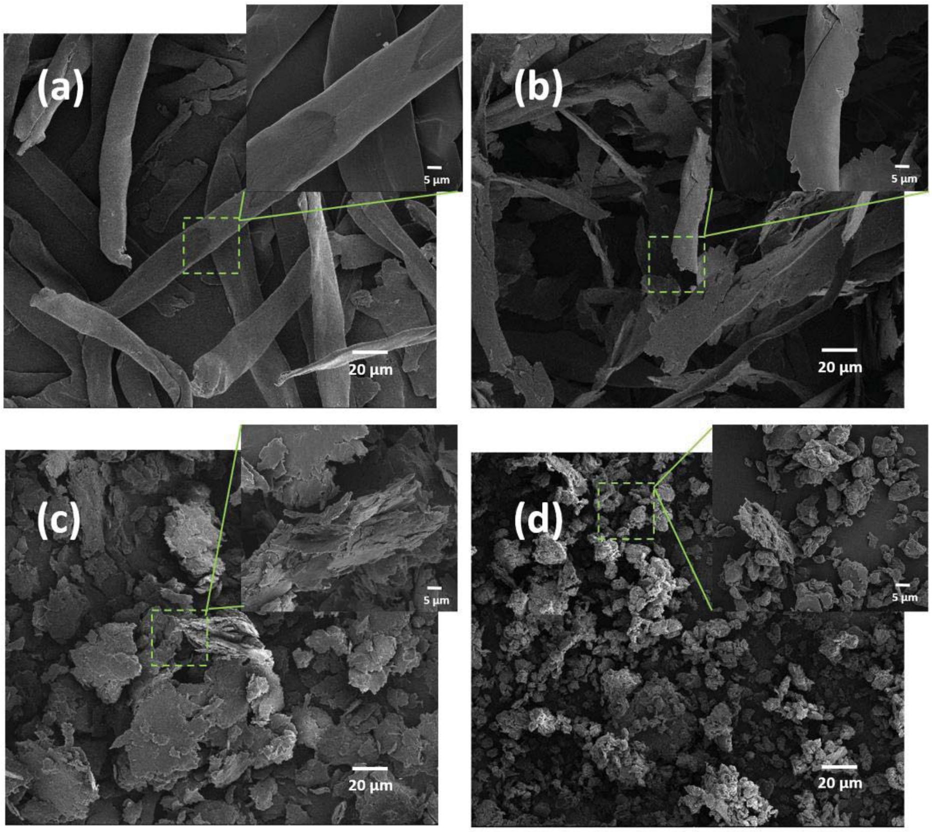

Fig. 2 SEM images of Wiley milled cotton (a) and cotton ball-milled for 15 min (b), 45 min (c) and 120 min (d). Scale barsin large images and insets = 20 µm and 5 µm respectively

down the fibers, lowering the sample birefringence as well as the average size of fibers. With longer milling time, the fiber shape disappeared for BMC-45 and BMC-120 (average sizes were 47 µm and 23 µm, respectively), indicating that the extended ball milling effectively broke the WMC fibers into smaller particles.

Figure 2 shows the FE-SEM images of the samples. Wiley milling chopped the cotton fibers into relatively large fragments of about 120 µm in length (Fig. 2a). A closer observation of a single fiber (zoomed in Fig. 2a) shows that the intrinsic fiber morphology of WMC remained intact. However, ball milling significantly degraded the fiber. Even 15 min of ball milling (Fig. 2b) split open some fibers along the fiber length as well as breaking some into small fragments. The fragments were irregular, but the longitudinal fragmentation was dominant. Ball milling extended to 45 min reduced the aspect ratio of the fragments to generate particles with a diameter of about 50 µm (Fig. 2c). However, some large particles remain in sample BMC-45, suggesting the inhomogeneity of cellulose fiber particles after ball milling. The size of the particles was further decreased to about 7 µm after 120 min of ball milling (Fig. 2d). The disordered fiber residues were approximately 10-15 μm in length (zoomed in Fig. 2d) with coarse surfaces and pores, showing the higher extent of destruction of the cotton fibers.

Molecular weights

Table 1 shows that the molecular weights of the samples decrease steadily with increased milling time. Some oxidation is revealed by the notably increased carbonyl amount from 1.9 μmol/g (WMC) to 36 μmol/g for BMC-120. As the chains became shorter, more carbonyl groups per unit mass appeared than the expected increase based on the increased number of reducing ends from breakage of the molecules. However, the oxidation resulted in only more carbonyls, whereas the amount of uronic acid groups did not increase significantly. The distributions of oxidized functionalities with regard to molar mass and the corresponding molar mass distributions are given in Fig. S2.

Table 1 The DP based on number-average molecular weight (Mn), weight-average molecular weight (Mw), Z-average molecular weight (Mz); sample polydispersity and calculated average molecular lengths of Wiley and ball-milled cotton cellulose

Samples	DP on number-average (Mn) [a]	DP on weight-average (Mw)	DP on Z-average (Mz)	Dispersity (Mw/Mn) [b]	Molecular lengths (nm) from Mn, Mw, Mz [c]
WMC	718	3335	5850	4.7	370 / 1718 / 3013

BMC-15	517	2143	4696	4.2	266 / 1103 / 2418
BMC-45	344	1409	3659	4.3	177 / 726 / 1885
BMC-120	265	856	2134	3.2	137 / 441 / 1099

[a] DP was calculated by equation (1)

[b] The dispersity equals Mw/Mn.

[c] The molecular lengths were calculated according to equation (2).

Specific surface area (SSA), pore size and thermogravimetric analysis (TGA)

SSA was determined from N_2 adsorption using BET analysis (Brunauer et al. 1938; Sehaqui et al. 2011). All samples presented similar adsorption isotherm curve shapes (Fig. 3a). WMC absorbed the lowest quantity of N_2. The highest absorption value was 5 cm^3/g for BMC-120. The SSA and average pore width are plotted in Fig. 3b based on the BET analysis. SSA showed a gradual increase with increased ball milling time. It can be explained by the destruction of cellulose structures after ball milling and exposure of internal surface of fibers as seen in the SEM images (Fig. 2).

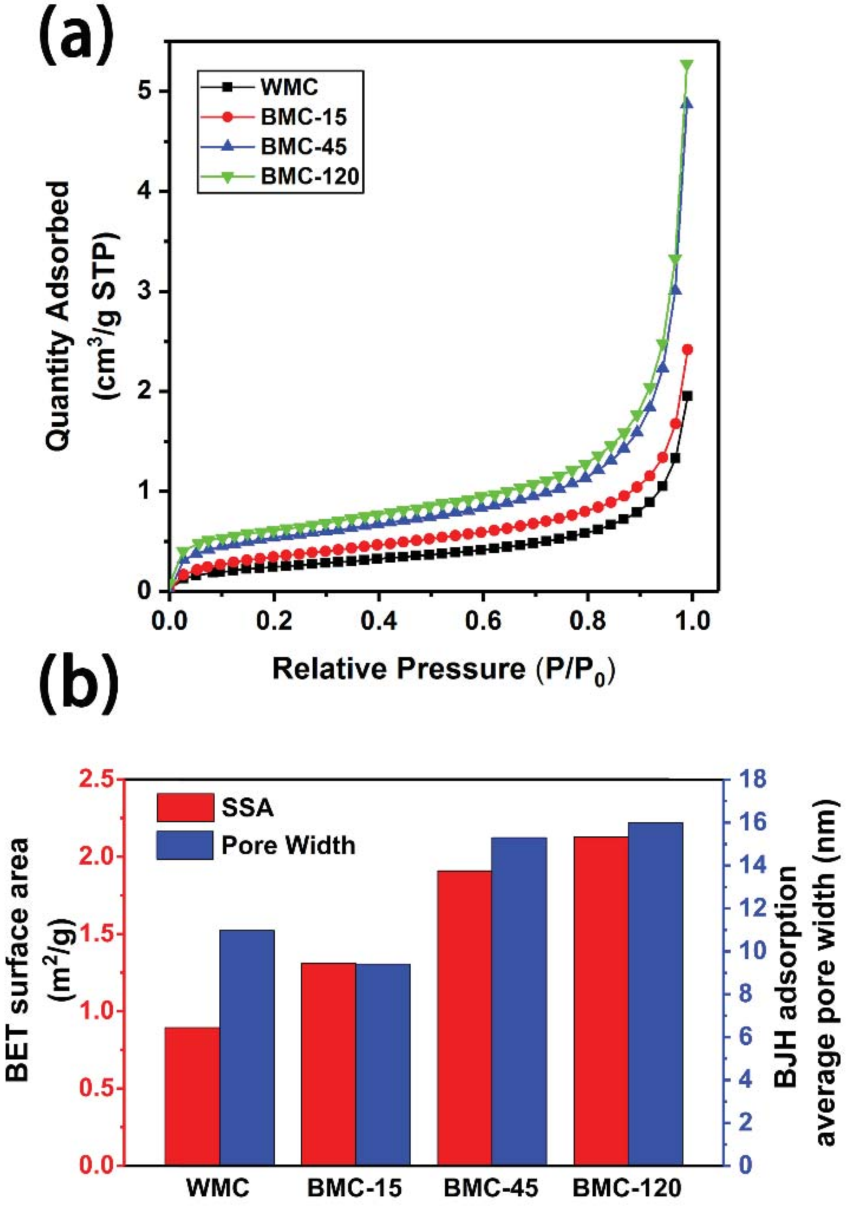

Fig. 3 The adsorption isotherms (a) and BET surface area (red bars in b), BJH adsorption average pore width (blue bars in b) of Wiley milled cotton cellulose and cotton cellulose ball milled for 15, 45 and 120 min

The average pore width decreased slightly for BMC-15 but the pores were opened significantly for BMC-45 and BMC-120 with approximately 15 nm of average pore width. As expected, the ball-milling treatment for longer times is an effective way to disrupt the ordered arrangements of cellulose molecules. It breaks down the fibrous structures, exposes more surface area, and opens the pores of cotton. The initial decrease in pore size may have resulted from impact compression by the ball mill without the damage and fragmentation that occur at longer ball-milling times.

The samples were studied by TGA and DTG under an N_2 atmosphere. All data were plotted in the TGA weight loss mode and the DTG mode. From the analysis of thermal properties, we can estimate the cellulose crystallinity according to Bertran and Dale (1986), who used DSC to show that the crystallinity of cellulose could be correlated with the moisture content. The hypothesis was that the amorphous region of cellulose should absorb more moisture in a humidity chamber, whereas the crystalline region adsorbs much less. Of course, there is a rough correlation between the initial moisture content and SSA.

The TGA and DTG results are displayed in Fig. 4. The point of rapid weight loss for WMC appeared at nearly 300 °C while the curves for BMC samples shifted left to lower temperatures (Fig. 4a). BMC-120 began degrading obviously at 250 °C and lost almost all of its initial weight, indicating a decrease of thermal

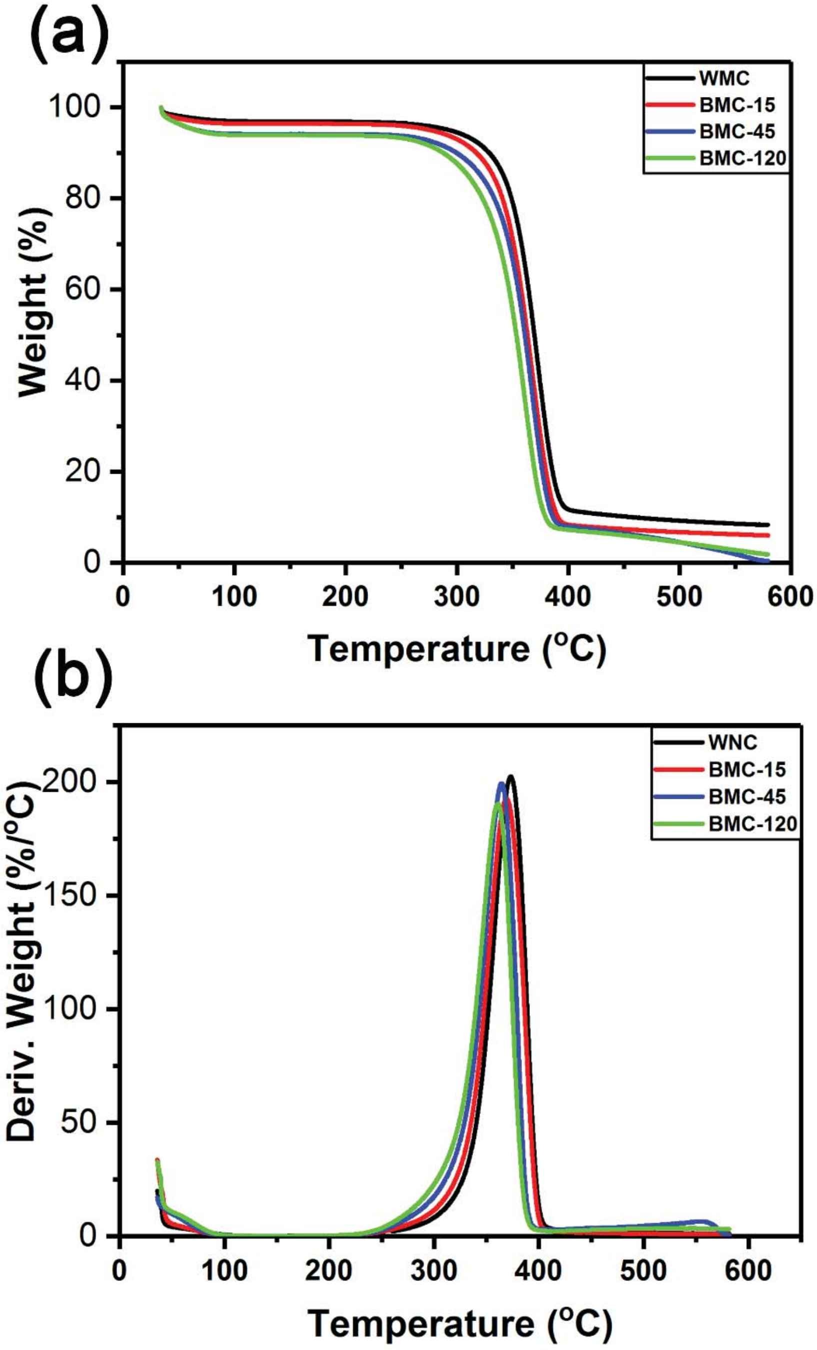

Fig. 4 TGA (a) and DTG (b) analyses of Wiley milled cellulose and ball-milled cellulose for different times

stability after ball milling. WMC showed the highest maximum degradation rate as well as the highest degradation temperature (Fig. 4b). With extension of ball-milling time, the temperature for maximum degradation rate reduced to 369.3 °C, 367.2 °C and 362.4 °C for BMC-15, 45 and 120 (Fig. S3a). However, the weight loss at each maximum DTG temperature showed a gradual increase (Fig. S3b), confirming the loss of stability after ball-milling treatments. This apparent loss could result, however, from a constant heating rate and the smaller particle sizes of the ball-milled materials. If the weight loss is taking place on the surfaces, larger crystals would take a longer time to decompose.

Two more correlations are shown for the four cotton samples (Fig. S4). The plots give the correlation of weight loss at 100 °C versus the temperature at the maximum degradation rate as well as the weight loss vs the maximum degradation rate. Both correlations are satisfactory ($R^2 = 0.99$ and 0.94, respectively) for the cellulose samples that were preconditioned in the humidity chamber. The good correlations of the ball-milling time duration with two parameters further suggest that the high moisture loss is from the amorphous material of BMC.

ATR-FTIR and FT-Raman spectroscopy

The FTIR spectra are shown in Fig. 5a. The spectrum for WMC showed infrared bands and peaks commonly observed for cotton: a wide OH stretching band (3600-

3000 cm^{-1}), a CH stretching region (3000-2900 cm^{-1}), the OH bending region, 1800–1300 cm^{-1}, and the fingerprint region with multiple combination bands, 1250–850 cm^{-1}. The visible bands at 3270 cm^{-1} and 710 cm^{-1} are typical for cellulose Iβ for WMC, even though there are tiny peaks at 3240 cm^{-1} and 750 cm^{-1} assigned to a small amount of cellulose Iα (Sugiyama et al. 1991). Ball milling leads to progressive broadening of the OH band, with the BMC-120 spectrum lacking the inflection points at 3334 cm^{-1} observed for WMC. Meanwhile, the bands attributed to both cellulose Iα and Iβ disappeared for BMC-120, a result attributed mainly to the destruction of the crystal structure by lengthy ball milling.

Ball milling also results in changes to the fingerprint IR region. While the position of the 1159 cm^{-1} peak is slightly altered by ball milling, its intensity appears unaffected. In contrast, the well resolved peaks at 1107 and 1052 cm^{-1} diminish in intensity for the sample ball-milled for 120 min. The prominent peak at 1029 cm^{-1} is gradually shifted to 1019 cm^{-1} following ball milling. Two shoulder bands are observed centered at 1000 and 985 cm^{-1} in the Wiley milled sample; however, only one shoulder band (995 cm^{-1}) is observed for BMC-120. The peak near 898 cm^{-1} appears more intense in the ball-milled cotton samples. An early study by Nelson and O’Connor (1964b) observed similar spectral changes in ball-milled cotton samples. Key changes include the position of the 1163 cm^{-1} band (observed in this study at 1159 cm^{-1}), and the intensity of bands at 1111 and 893 cm^{-1} (observed in this study at 1107 and 898 cm^{-1}, respectively). Their study did not show significant changes to the 1052, 1000 and 985 cm^{-1} bands, but these

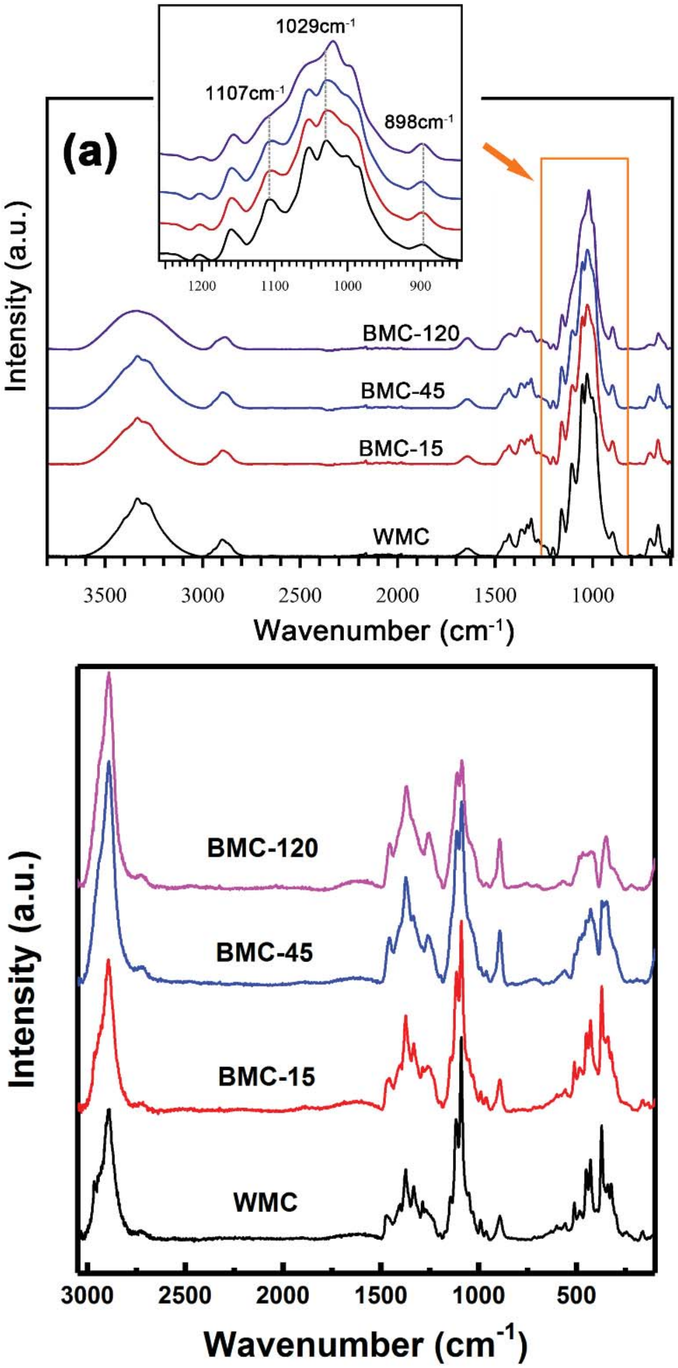

Fig. 5 ATR-FTIR (a) and FT-Raman (b) spectra of Wiley milled cellulose, and cellulose ball-milled for 15 min, 45 min and 120 min. A small peak for water in amorphous domains is seen at ~ 1650 cm^{-1}.

differences could be the result of their sampling methodology and resolution of their instrument.

The Raman spectra of Wiley and ball-milled cotton cellulose are presented in Fig. 5b. With the increase of milling time, the main peak of cellulose at 380 cm^{-1} assigned to symmetric bending vibration of pyranose rings in crystalline cellulose showed visible reduction together with the C-O-C and C-H stretching vibration at 1096 cm^{-1} and 2900 cm^{-1}, respectively (Agarwal and Ralph 1997; Agarwal et al. 2016; Makarem et al. 2019). The decreases of these main peaks were substantial for BMC-120, indicating the distortion of crystalline arrangements and the smaller CrI. Meanwhile, the peaks attributed to the bending vibrations of cellulose glycosidic linkages (990 cm^{-1}, 1116 cm^{-1} and 1331 cm^{-1}) disappeared for the most amorphous sample (BMC-120) (Wiley and Atalla 1987).

The notable peak of 1481 cm^{-1} in WMC shifted to 1462 cm^{-1} with prolonged ball milling. The ratio of these two peaks refers to the proportion of crystalline cellulose, and confirmed an increased amorphous fraction in the sample, leading to a significant decrease of CrI (Schenzel et al. 2005).

SFG analysis

SFG spectroscopy is specific to non-centrosymmetric vibration modes in an otherwise amorphous matrix (Barnette et al. 2011). The SFG signal intensity can be used to quantify the amount of crystalline cellulose in the sample if a proper calibration curve can be obtained (Barnette et al. 2012; Park et al. 2013). For ball-milled cellulose, the main features observed in the CH stretch region (2800-3000 cm^{-1}) are the peak at 2850 cm^{-1} assigned to the CH_2 symmetric vibration, the peak at 2944 cm^{-1} as the CH_2 asymmetric vibration, and a shoulder at 2968 cm^{-1} also assigned to CH_2 asymmetric vibrations (Fig. 6a) (Lee et al. 2013). Time-dependent density functional theory (TD-DFT) calculations also revealed that the CH_2 vibrations between 2800-3000 cm^{-1} are highly coupled with CH vibrations on the six-atom ring (Lee et al. 2016a). Thus, the peaks in this region represent more than just the vibrational modes of isolated CH_2 groups. The peak at 2944 cm^{-1} is characteristic for cellulose Iβ, which also has a shoulder at 2968 cm^{-1} (Huang et al. 2018a). With increased ball-milling time, peaks between 3200-3500 cm^{-1} assigned to the stretching vibrations of OH groups in cellulose Iβ show a notable decrease. Note that OH peaks in this region also cannot be assigned to single vibrational modes; they originate from highly coupled vibrations of multiple OH groups in cellulose structure (Lee et al. 2015b). Meanwhile, the broad component at 3450 cm^{-1} can be attributed to OH groups exposed at the surface of cellulose crystals (Makarem et al. 2017).

Fig. 6b displays changes in the total intensity of the CH/CH$_2$ SFG peak as a function of ball-milling time. The SFG intensity from the cellulose Iβ phase in the BMC-15, -45, AND -120 samples decreased to ~35%, ~9%, and ~1%, respectively, compared to the SFG intensity of WMC. This implies that a small fraction of cellulose Iβ crystallites still remains in BMC-120.

Another important aspect is that the shape of the CH/CH$_2$ asymmetric stretch feature in the 2900-3000 cm^{-1} region changes with ball milling. The relative intensity ratio (2968 cm^{-1}/2944 cm^{-1}) is plotted against the right-side red axis in Fig. 6b. The increase in this ratio implies that a small fraction of cellulose Iβ was converted to cellulose II, as also found for the FTIR work. This transformation might have happened when the amorphized portion of cellulose chains underwent crystallization due to the proximity of cellulose chains or mechanochemical processes during ball milling.

SFG peaks in the OH stretch region (3200-3600 cm^{-1}) can be deconvoluted with various components. The component at 3270 cm^{-1} is characteristic of cellulose Iβ. The fraction of this component intensity with respect to the entire OH components (f_β) can show the change in cellulose I_β fraction among the SFG-active fraction of cellulose. The plot of f_β versus the milling time is also shown in Fig. 6b, decreasing as the ball-milling time increases.

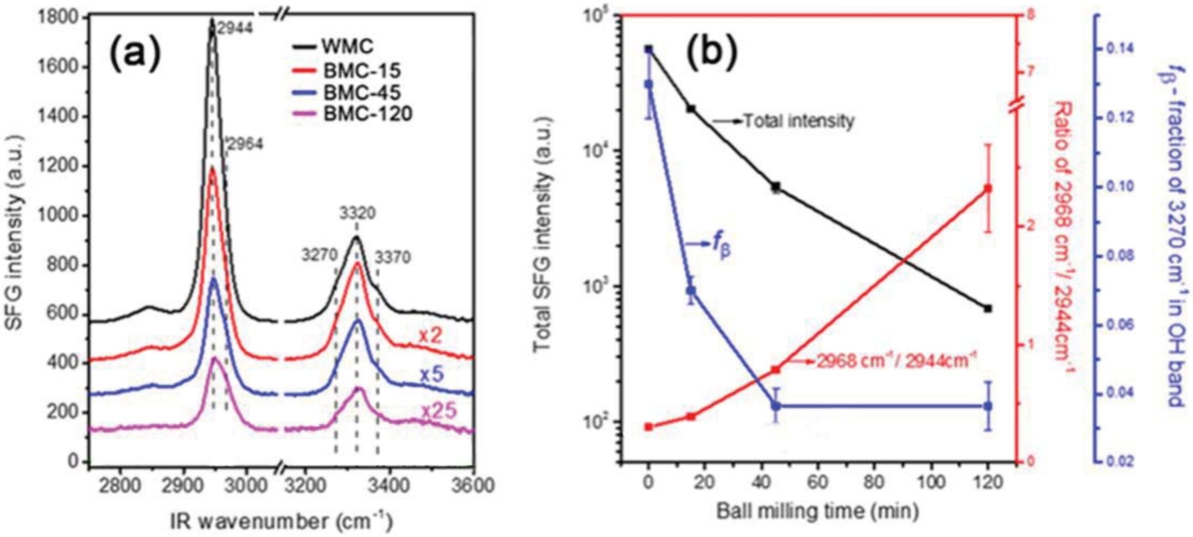

Fig. 6 (a) SFG spectra of cotton before and after ball milling for 15 min, 45 min, and 120 min. Note that some spectra are amplified for comparison with different magnification ratios (marked for each spectrum). (b) Plots of the SFG total intensity, the 2968cm^{-1}/2944cm^{-1} intensity ratio, and the 3270 cm^{-1} fraction in the OH peak versus the ball-milling time

NMR characterization

The standard ^{13}C CP spectra of WMC and the three BMC samples show that cellulose crystallinity decreases with longer ball milling by the sequential reduction in the intensity of crystalline cellulose C-4 at 88-90 ppm and the rise of disordered cellulose C-4 at 80-85 ppm. Peak multiplicity was observed in WMC since both Iα and Iβ cellulose contain two magnetically inequivalent glucose units: A and A' for Iα and B and B' for Iβ (Fig. 7) (Kono and Numata 2006). For BMC-45, the sharp peaks become negligible: instead, the spectra are dominated by broad components originating from the disordered forms (D), the intensity of which was low in the Wiley milled sample.

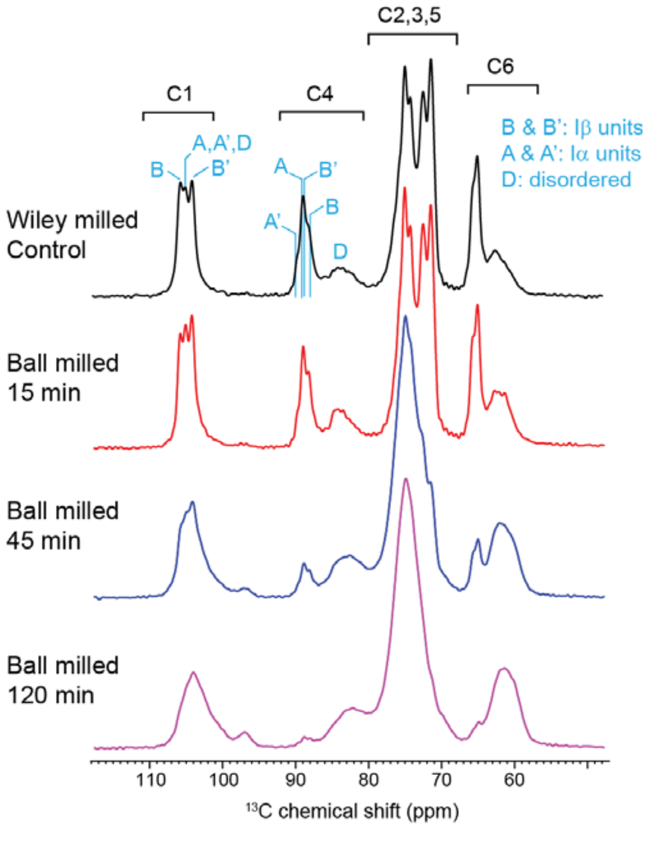

Fig. 7. ^{13}C CP spectra of Wiley milled control and ball milled cotton samples. Representative signals of the inequivalent glucose units in Iα and Iβ cellulose are labeled in cyan for the control sample

Spectral deconvolution allows us to analyze the composition and crystallinity of cellulose in greater detail and as a function of ball-milling time. The peak positions are using those resolved in the 2D ^{13}C-^{13}C correlation spectra of these unlabeled samples as enabled by the sensitivity-enhancing Dynamic Nuclear Polarization (DNP) technique, the spectral and technical details of which are reported in a separate article in the same issue (Kirui et al. 2019). The simulated and measured spectra dovetail well (Fig. 8a). In contrast, the central peak position for the disordered part gradually shifted from 85 ppm in WMC to 82 ppm in BMC-120. Quantification of peak areas shows that the cellulose crystallinity decreases in the order of 68%, 58%, 28% and 13% in the four samples, which clearly reveals the molecular-level structural effect of ball milling (Fig. 8b).

A central question is whether the crystallites of cellulose fracture homogeneously or not. This was addressed by monitoring the intensity change for the highly disordered form (Hd) at 82.5 ppm, which is only a minor component in the Wiley milled cotton but becomes dominant after 2 h of ball milling, accounting for one-fifth of all cellulose (Fig. 8c). If structural fractioning of the crystallites occurs progressively, we expect the size of cellulose particles to be roughly consistent within each step, a scenario in which the most disordered molecular structures can only occur in the last step (Fig. 8d). In contrast, linear growth of the highly disordered subform is expected for inhomogeneous fractioning, in which large and small particles could coexist. The experimental results align better, although not perfectly, with the second model, suggesting that cellulose crystallites are perturbed inhomogeneously during the ball-milling process. This concept of inhomogeneous decrystallization is also supported (at a much larger length scale) by the imaging results presented in Fig. 2 and Fig. S1.

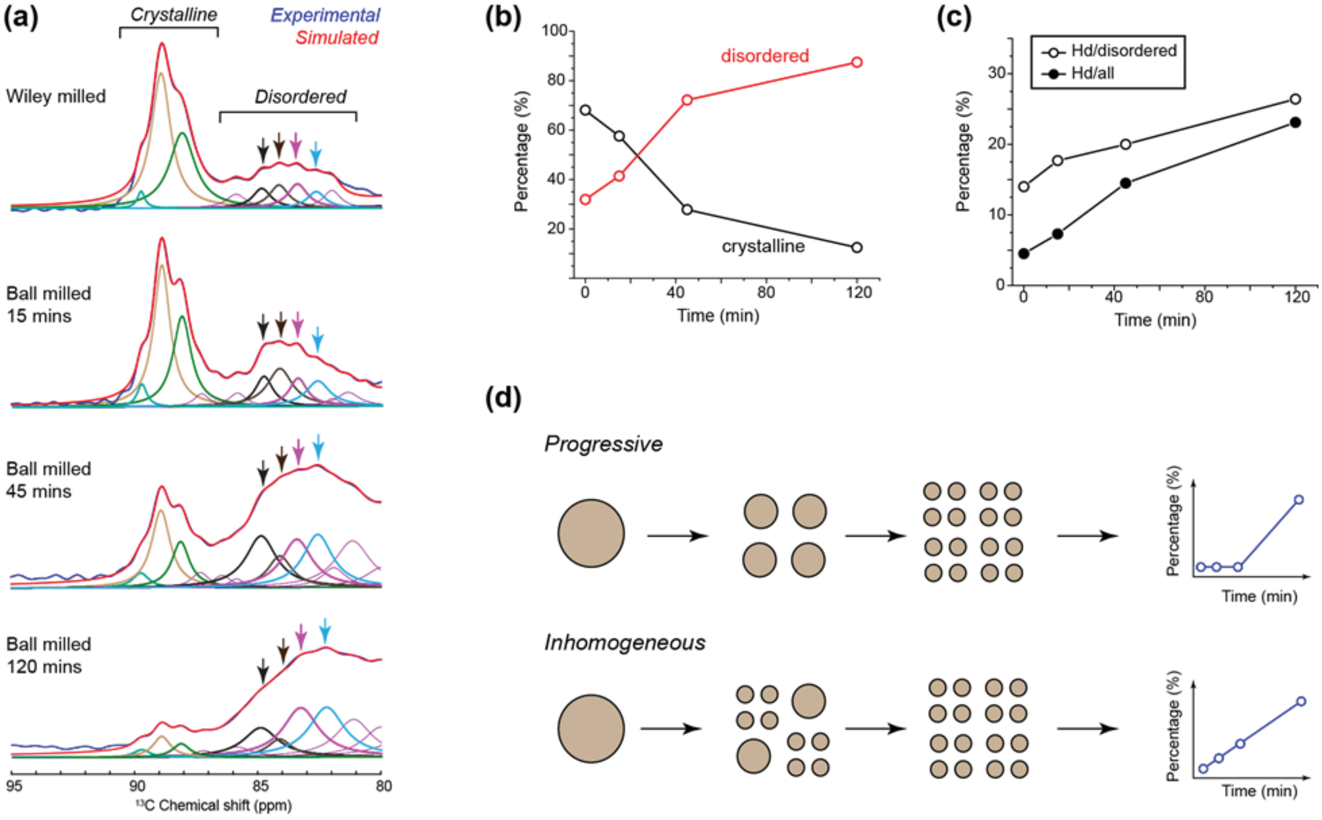

Fig. 8. Compositional change of cellulose during ball milling. (a) Cellulose compositional change tracked by spectral deconvolution. (b) Quantification of cellulose crystallinity. (c) The content of highly disordered (Hd) allomorph (82.6 ppm) increases with longer duration of ball milling. (d) Two models for cellulose

fractioning during ball milling. The NMR data in panel (c) support inhomogeneous fractioning

Laboratory and synchrotron X-ray diffraction analyses

Because of the fundamental problems with the conventional methods (see Introduction), we have used only the Rietveld method to analyze the crystallinity of the samples. Crystallinity was analyzed with laboratory (reflection mode) and synchrotron (transmission mode) X-rays. All data were corrected by subtracting background due to the air scatter and sample holder and, for the synchrotron work, the capillary. The patterns are compared in Fig. 9. WMC gave typical cellulose Iβ X-ray patterns with major peaks at 14.8°, 16.5°, 22.5° and 34.5°, respectively attributed to the (1-10), (110), (200) and (004) reflections (Fig. 1 shows that each of these peaks [especially (004)] is a composite of one or more adjacent peaks.) The slightly lower 2θ value (22.5°) for the (200) reflection of the control cotton compared to the 23.0° value for the archetype tunicate structure indicates a larger d-spacing, perhaps resulting from the reduced long-range forces in the smaller crystallites of cotton. Also, there may be strains on the crystallites because of their participation in the complex cell wall architecture that results in a disrupted structure compared to the higher order of the tunicate nano-needle crystallite films (see Fig. 6 in Huang et al., 2018b). The synchrotron X-ray pattern of WMC

(WMC-S in Fig. 9) presents a few more peaks than the laboratory pattern WMC-L. The two overlapping peaks at 20.3° and 20.6° are assigned to the (012) and (102) reflections (Fig. 1). The near absence of those “shoulder” peaks near the (200) peak on the WMC-L pattern indicates preferred orientation of the crystallites (French 2014) despite the sample simply being sprinkled on the diffractometer’s rotating sample holder and pushed towards the center with a spatula.

As the ball milling progressed, the maximum intensity decreased for these patterns (Fig. 9), which are plotted with constant areas between the curve and the baselines (not shown). Instead, the photon counts (X-ray intensity values) were slightly higher in most places to compensate for reduced (200) peak height. Under these conditions of constant (intensity × 2θ°) area it is legitimate to state that higher peaks indicate higher crystallinity. The pattern for BMC-120 is similar to those in studies on amorphous cellulose produced with different kinds of solvents (Schroeder et al. 1986; Isogai and Atalla 1991; Rollin et al. 2011).

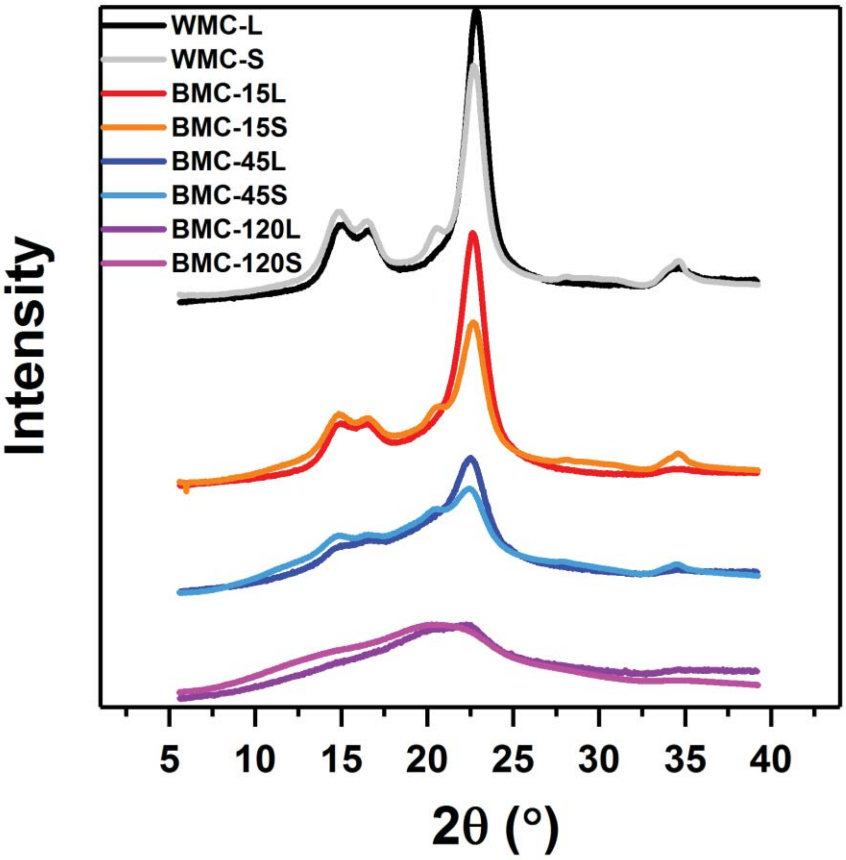

Fig. 9 Laboratory (L) and CAMD synchrotron (S) X-ray patterns for the samples. For comparison, the intensities were adjusted to have comparable area under the curves, with compensation for the different wavelengths and step sizes

Rietveld analyses were performed to obtain more detailed information from laboratory and synchrotron X-ray patterns (Fig. 10). All the samples show fairly good fits of the calculated patterns to the experimental patterns in the images a-h.

The thin red lines (representing the crystalline Iβ component) indicate reduced peak heights and areas under the curve as the ball-milling time increased. Meanwhile, the areas under the green lines, representing the quantity of amorphous cellulose, were progressively greater proportions of the total. The crystallinity index (CrI) values calculated from the Rietveld refinement are also shown in Fig. 10. WMC had CrI values of 88.7% for the laboratory XRD data and 62.1% for the synchrotron data. The relatively lower value of CrI from the synchrotron analysis is possibly a consequence of the inhomogeneity of the sample. Particle sizes were not uniform. Importantly, these crystallinity values are based on values of intensity for the calculated components exported from MAUD. MAUD also presents percentages of each phase in the program interface with typically very high error limits. Those values can differ substantially from the percentages calculated from the areas under the curves plotted in Fig. 10. Rietveld CrI analyses of BMC-15 and BMC-45 gave similar values regardless of X-ray source (laboratory and synchrotron). Those CrI are around 50% and 30% respectively. The amorphous phase dominated the patterns for BMC-120, with fairly similar CrI values of 13.2% and 5.2%. As in the SFG and NMR results, X-ray diffraction indicates that not all of the cellulose I crystallinity was destroyed even after 120 min. This is in contrast to the conclusions of Millett et al. (1979) who obtained similar diffraction patterns and used the Segal method. Comparison of the BMC-120 patterns in Fig. 9 and 10 emphasizes how the visual impression of the nature of the diffraction pattern can change depending on the amplitude of the y-axis for intensity. The Rietveld method is immune to visual impressions and it gave results for BMC-120 that are more consistent with the SFG and ssNMR results.

The 2D synchrotron X-ray diffraction images are also shown in Fig. 10 to the right of the 1D patterns obtained from the XRD2DScan program. The black experimental line in Fig. 10b (underneath the blue fitted line), for example can be considered to be the result of scanning to the right from the center of the adjacent 2D pattern. The 2D image of BMC-15 shows an uneven intensity distribution proceeding around the rings at the same 2θ angle (Fig. 10, row 2). This is another example of preferred orientation, which occurred for the sample in the capillary tube for the synchrotron. The pattern is very similar to those from cotton fiber bundles (French and Kim 2018) although the sample consisted of particles picked up with tweezers and pushed into a capillary tube. (It was difficult to ensure good sampling for these small samples.) This underscores the need to take measures to avoid preferred orientation and to be aware that it may be inconsistent from sample to sample. In the present laboratory experiments, the sample holder was rotated during data collection. In the synchrotron experiments, the data were averaged around each circle to get the 1D plots.

In this work, the amorphous material was modeled by a very small crystal of cellulose II (Langan et al. 2001), initially 12 Å in each direction. The calculated scattering is somewhat different from that of cellulose Iβ and seem to fit the observed data better. Rietveld refinements that include this model for amorphous material can vary the same parameters as are varied for the crystalline phase, providing the needed variability to compensate for differences in amorphous material.

In our earlier Rietveld analyses of cellulose, we had not corrected the experimental data for the background scattering. In those cases, the background was instead included as part of the Rietveld refinement, based on a quadratic equation. In a number of cases, the refined amorphous component of the calculated intensity and the refined background worked together to give a better fit to the observed data but the values for the background were negative in some 2θ ranges. Subtraction of carefully collected background data from the experimental data allowed the Rietveld refinement to avoid the unphysical results because the background was simply not included and reduced the number of variable parameters by three.

729

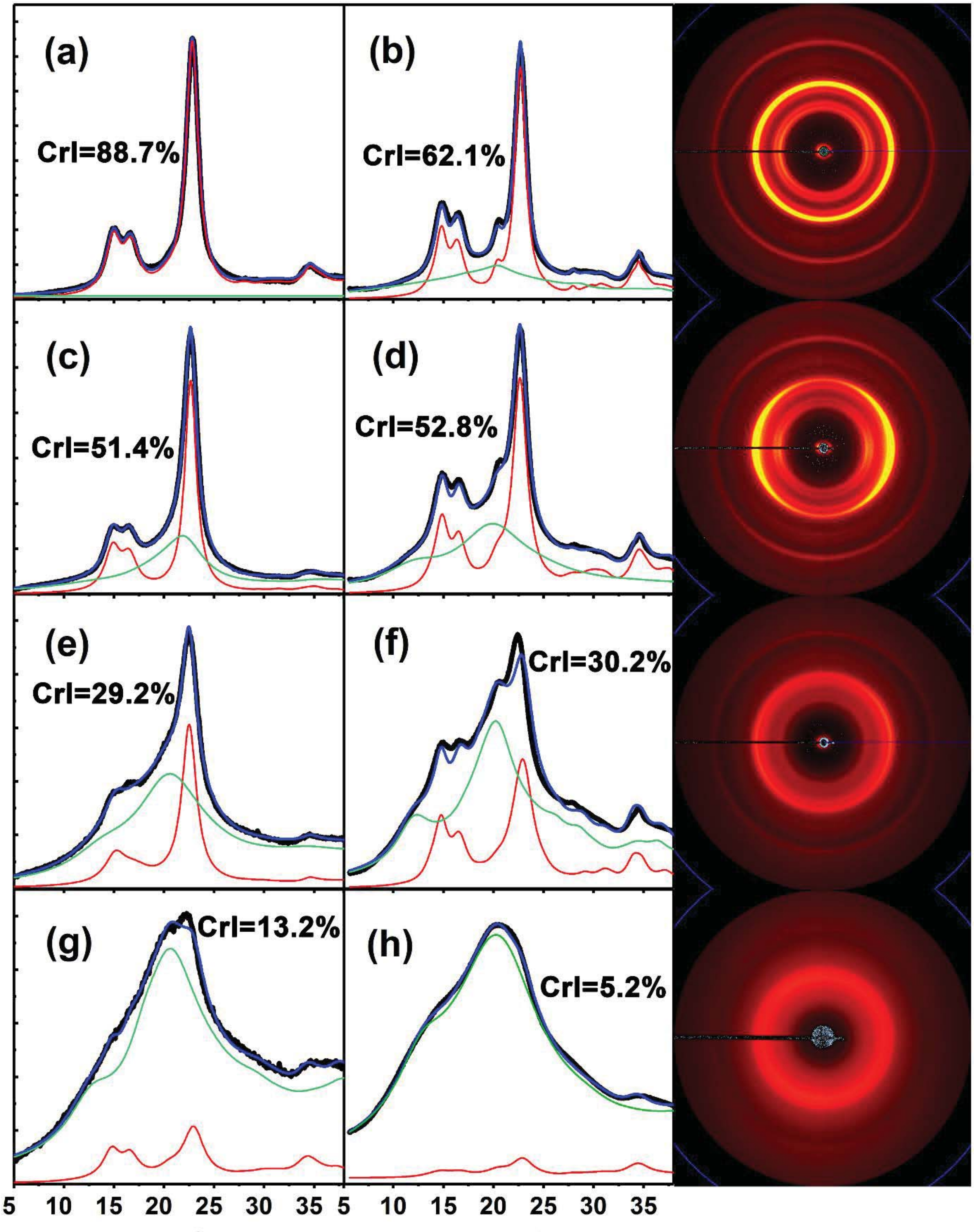
(a)
CrI=88.7%
(b)
CrI=62.1%
(c)
CrI=51.4%
(d)
CrI=52.8%
(e)
CrI=29.2%
(f)
CrI=30.2%
(g)
CrI=13.2%
(h)
CrI=5.2%
5
10
15
20
25
30
35
2θ (°)

Fig. 10 Rietveld refinement analyses of laboratory (a, c, e and g) and synchrotron X-ray results (b, d, f and h) for WMC (a, b), BMC-15 (c, d), BMC-45 (e, f) and BMC-120 (g, h). Black lines are the experimental 1D data; blue, red, and green lines refer to the total fitted line for the analysis, and the modeled crystalline cellulose Iβ and modeled amorphous cellulose contributions, respectively. Backgrounds were experimentally determined and subtracted. The 2D synchrotron X-ray diffraction images related to each sample are plotted to the right of the patterns. The yellow circles or arcs indicate the greatest intensity. Very small gray dots in the beam stop and support areas indicate negative intensity values resulting from background subtraction. They are within the noise levels

The crystallite sizes perpendicular to the (200) planes (Fig. 11) were obtained from the fitted cellulose Iβ patterns with the MAUD software. However, the Scherrer equation was applied, rather than MAUD crystallite size values, which are somewhat larger than those calculated with the Scherrer equation. The calculation regions were set at $2\theta=20°-25°$, in which the (200) plane of cotton cellulose is included. Both the laboratory and synchrotron X-ray methods showed that the ball-milling treatment not only reduced the fraction of crystalline material but effectively reduces the crystallite sizes (Fig. 11). The trend is in agreement with the decrease of the CrI discussed above but there is better agreement between laboratory and synchrotron results for crystallite size. Diffraction-based determinations of crystallite size are minimum values because the peak widths are affected by the other factors (Huang et al. 2018b).

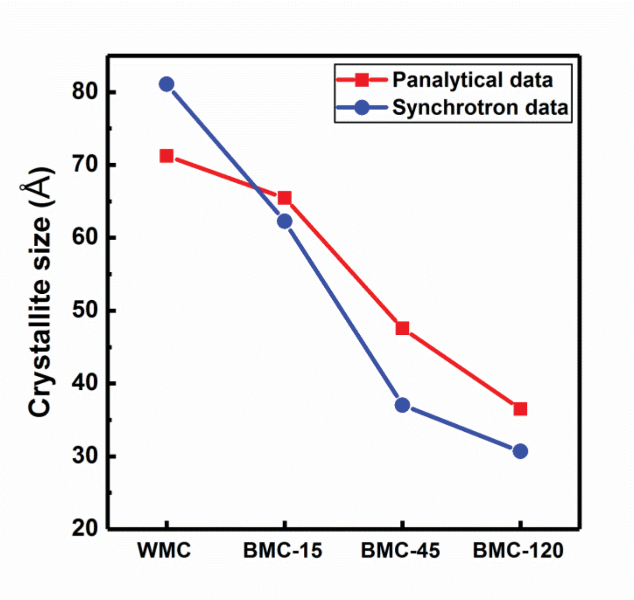

Fig. 11 Crystallite sizes perpendicular to the (200) reflections of Wiley milled and ball-milled cotton cellulose determined by laboratory XRD and synchrotron XRD

The various shapes of the calculated cellulose Iβ and amorphous contributions to the total modeled diffraction intensity have arisen because they are the results of answering the question, "What must be done to the shape of an ideal cellulose diffraction pattern to make it match the experimental one?" Ideally, the individual components would vary in simple ways, such as total number of counts that represent the fraction of total intensity contributed by the component. However, that is not enough variability. The widths of the resolved Iβ component are sharper for the WMC than the BMC, so that must be considered. The laboratory samples clearly have preferred orientation; MAUD can model that component with the March-Dollase equation (Dollase 1986) that changes the intensities of the individual peaks. In the end, to obtain low values of the discrepancy indices (R values), the variations of crystallite size in the different dimensions was also modeled (Popa and Balzar, 2008) that add considerably to the number of variables that were used.

Comparison of the methods

A comparison of crystallinity estimates from each of the surveyed methods was undertaken. Although the different analyses in this work measure different properties (Lee et al. 2016b), it is of interest to know how well they agree on the degree of disruption of the structure of the cotton fiber caused by ball milling. In the case of diffraction, we have used a two-phase model that considers both the fraction of amorphous material and the size of the remaining crystalline material. The NMR work indicates the relative fractions of molecules in characteristic environments. Various methods for calculating CrI have been proposed for IR and Raman data, and are employed in this study. SFG-based crystallinity determinations have also been reported, but absent a calibration curve, we assigned a value of a 100% for the CrI of WMC.

For the other analyses, we are not aware of existing crystallinity indices based on, for example, carbonyl group increases. Such CrI values would not be widely applicable as there are many reasons that the carbonyl groups could have increased such as intentional oxidation reactions that do not affect crystallinity so much. Still, we felt that it was of interest to derive simple equations that would enable us to compare the crystallinities based on different methods. These relationships are tabulated in Table 2 and plotted in Fig. 12b.

Table 2 includes the results from a second, more conventional ^{13}C NMR analysis (Larsson et al. 1999; Massiot et al. 2002) that is fully reported in Supplementary Information. The values of crystallinity in Table 2 for the conventional NMR method were calculated from the sums of the percentages for the four NMR peaks: Iα, I(α+β), Iβ, and the paracrystalline peak (Foston et al. 2011; Park et al. 2010). For this conventional method, the ssNMR crystallinity values for the WMC and BMC-15 are very similar, but the BMC-45 and BMC-120 results diverge considerably. This result might be partially attributed to water swelling in the conventional ^{13}C NMR samples as part of their preparation. That could lead to some recrystallization or other change in the molecular organization.

Every surveyed method for estimating sample crystallinity showed a decrease in value that followed increases in ball-milling time (Table 2, Fig 12). (The pore size measurements, which showed a decrease for BMC-15 and subsequent increases, were not included.) For example, the WMC samples were more crystalline by any measure than any of their corresponding BMC samples in Fig. 12. Omitting from Fig. 12a the water-soaked conventional ssNMR results and the SFG data, the agreements among the methods is considerably improved. The outlier here is the synchrotron result for WMC. As seen in Fig. 10, the laboratory and synchrotron diffraction patterns differed substantially, most apparently because the laboratory data exhibit preferred orientation of the crystallites. In theory, the results of these two X-ray techniques should agree, and pursuit of the experimental protocols and algorithmic factors in the analysis should improve the inter-method agreement and improve the accuracy of X-ray crystallinity measurements.

Table 2 Comparison of numeric crystallinity values and underlying data

	Laboratory XRD	Synchrotron XRD	ss-NMR	ss-NMR[a]	FTIR	Raman	SFG
Methods	MAUD Rietveld method	MAUD Rietveld method	Cr 88-90ppm Am 80-85ppm	Fitting and modeling of NMR spectra[a]	CrI=$A_{1372\ cm^{-1}}/A_{895cm^{-1}}$	CrI=[($I_{380\ cm^{-1}}/I_{1096\ cm^{-1}}$) -0.0286]/0.0065	SFG total intensity
Reference	Lutterotti et al. 2007		Kono and Numata 2006	Massiot et al. 2002	Oh et al. 2005	Agarwal et al. 2014	Kim et al. 2015
WMC	88.7%	62.1%	68%	67.5%	72.7%	78.6%	100%
BMC-15	51.4%	52.8%	58%	59.2%	56.9%	56.3%	35%
BMC-45	29.2%	30.2%	28%	45.3%	34.5%	40.4%	9%
BMC-120	13.2%	5.2%	13%	30%	10.7%	13.4%	3%

Samples	**SSA**	**Est CrI**	**DTG**	**Est CrI**	**Carbonyl**	**Est CrI**	**DP (Mn)**	**Est CrI**
WMC	0.8937	87.6%	371.99	95.8%	1.9	88.1%	718	86.3%
BMC-15	1.309	40.8%	369.32	57.9%	15	48%	517	52.8%
BMC-45	1.909	19.2%	367.18	34.3%	21.5	37.5%	344	24%
BMC-120	2.1265	15.4%	362.36	3.7%	36	23.8%	265	10.8%
Estimation Methods	CrI (%)=70/SSA^2		CrI (%)=$(DTG-360)^2/1.5$		CrI (%)=120000/$(Carb+35)^2$		CrI (%)=(DP-200)/6	

[a] Conventional SS-NMR method, reported in Supplementary Information

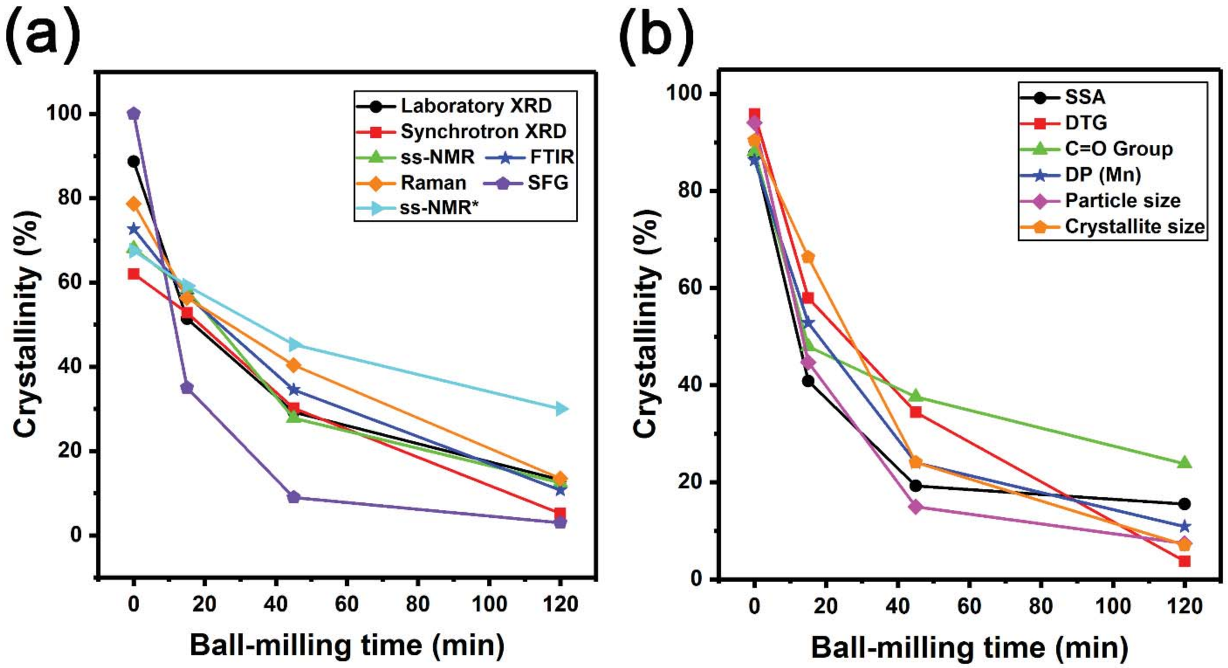

Fig. 12 Plots to compare crystallinity indices from different methods. (a) Those with established relationships. ss-NMR* denotes the conventional NMR analysis (b)Those with proposed relationships from Table 2.

Five different FTIR peak ratios have been proposed to predict crystallinity of cellulose. Those crystallinity values derived from the ratios in Table 3 are plotted in Fig. 13. It seems that the A1372 cm^{-1}/A2900 cm^{-1} ratio and the 1.06 *A1280 cm-^{1} /A1200 cm^{-1} +0.19 equations result in estimates of a too-narrow range of values. Similarly, the Liu et al. method (2012) estimates do not cover enough of the range for the BMC samples. One of the ratios of the Oh et al. studies showed crystallinity values comparable to the other methods reported in Table 2.

Samples	A1372 cm^{-1}/A895 cm^{-1}	A1430 cm^{-1} /A895 cm^{-1}	A1372 cm^{-1}/A2900 cm^{-1}	(1.06*A1280 cm^{-1}/A1200 cm-^{1})+0.19	(A708 cm^{-1}-A800 cm-^{1})/(A730 cm^{-1}-A800 cm^{-1})
WMC	72%	74%	100%	45%	59%
BMC-15	56%	35%	92%	34%	12%
BMC-45	34%	33%	75%	32%	9%
BMC-120	10%	10%	61%	29%	1%
Reference	Oh et al. 2005		Nelson and O'Connor 1964b	Ilharco et al. 1997	Liu et al. 2012

Table 3 Calculations of crystallinity based on FTIR results

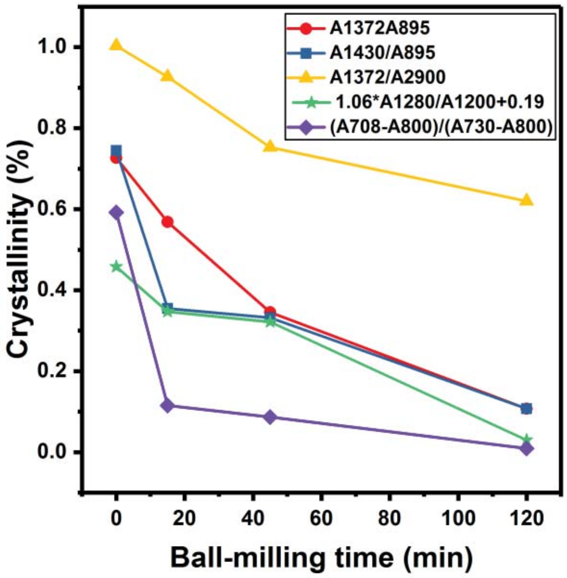

Fig. 13 Comparison of crystallinity indices from various infrared peak ratios (see Table 3)

Conclusions

In this work, cotton cellulose was ball-milled for 15, 45 and 120 min. Multiple approaches concurred that the cellulose crystals were progressively destroyed by the blunt-force impacts of ball milling. The fibers were split open and broken into small bits, the molecular weights decreased, and the cellulose was oxidized on a small scale, as shown by an increase in carbonyl groups. This resulted in more pores and higher surface area of the ball-milled cellulose. There was an increase in water adsorption and a decrease in thermal stability.

According to an average of the two different sets of diffraction experiments, the ball mill reduced the crystalline content of the original cellulose from around 75% to 9%. Ball milling also reduced the crystallite size of the decreasing amount of remaining crystals from about 75 Å to about 35 Å. Except as described below, none of the other results contradicts these basic conclusions.

Results from two other approaches are strongly influenced by neighboring molecules over a range of distances: sum frequency generation vibrational spectroscopy, and ssNMR. They gave reasonable correlations with the X-ray data but the language of the description of decrystallization is different. In the case of SFG, the intensities of the peaks in the OH- and CH- stretch regions decline because of a loss of dipole moment as the sample is decrystallized. In the unmolested crystals of cellulose Iβ, the molecules have parallel packing that results in net dipoles for the crystals. In the case of cellulose II, the individual molecules alternate in packing direction (antiparallel), so there is no net dipole and the SFG spectrum disappears. Somehow, the milling reduces the sizes of the parallel-chain domains, not only by fracturing the parallel-chain crystals of cellulose I, but also by mixing the fragments of adjacent crystallites that have antiparallel orientation (see Introduction), similar to the mercerization treatment but dealing presumably with crystal fragments rather than individual molecules.

NMR results, informed by the 2D results in the following paper, gave a surprising result. Namely, there are new molecular structural features created by the ball milling. Although the 1D NMR spectra appeared to experience a general broadening of the peaks as milling progressed (as did the FTIR and Raman spectra), the 2D NMR results could be resolved in terms of peaks that had narrow peak widths. The major ordered component of the 120 minute-ball-milled sample is similar to one of the cellulose Iβ molecules in tunicate cellulose. The major disordered components were most similar to surface molecules of native celluloses that have small crystals (*Arabidopsis, Brachypodium, Zea mays*). Remarkably, the native control cotton did not give peaks with chemical shifts closely similar to those interpreted from the small-crystal plant celluloses. Instead, the control cotton was analyzed in terms of molecular structural species similar to the archetypical

Cladophora A, A', and tunicate B and B' molecules. In the case of the 120-min ball-milled sample, there were also signals representing four different molecular species. We have not developed any ideas about the domain sizes needed to support the observation of four distinct molecular species by ssNMR in the small (30 Å) remaining crystallites or in the amorphous domains that were modeled with crystals of about 12 Å.

Another important finding from the DNP work was that the curve resolution did not depend on a “paracrystalline” component. The more conventional NMR analysis indicated a 27% paracrystalline component for the control cotton, but values of 18.6, 18.9, and 9.7% for the 15-, 45-, and 120-min samples respectively, in complete disagreement with the other analysis. The conventional NMR analysis also reported a large component of inaccessible fibril surface with a very broad width (about 3 ppm). Those values were 15.2, 22.4, 31.5, and 32.5% of the material. There was no need to invoke such a broad peak in the DNP work, nor did the observed increase in BET surface area support the modeled increase of inaccessible surface. Some of the other indicators of crystallinity from FTIR spectroscopy did not perform well enough either.

Ball-milled cotton was an interesting sample for analyses of amorphous or non-crystalline cellulose because few other molecules such as hemicellulose or lignin were present. Its initial crystal size is apparently bigger than for many other plants. Also, all of the samples had the same history until the ball milling began, rather than choosing native materials from different sources to obtain different crystallinities. The choice of cotton balls from Wal-Mart balanced trivial expense and wide availability against a lack of detailed sample history, but they should be similar to other samples of bleached and scoured upland cotton. The diffraction data for the samples is provided in Supplementary Information.

Future efforts could aim to improve the understanding of domain sizes (and size distributions) for the SFG and NMR signals. From the diffraction side, it may be that improvement of the model crystals is necessary to get a better agreement with the observed data. Perhaps more than two crystallite sizes will be needed to reflect a range of crystallite sizes. Also, is it necessary to employ the random quarter-up or quarter-down shifting of molecules described by Driemeier and Francisco (2014)? How do structures of crystals in the common plants with smaller crystals differ from being smaller pieces of tunicate crystals?

Acknowledgments

The authors gratefully acknowledged the support by Chinese Scholarship Council (CSC No.201706510045) for ZL. The NMR work was supported by National Science Foundation (NSF OIA-1833040). The SFG work was supported by the Center for Lignocellulose Structure and Formation, Energy Frontier Research

Center funded by the U.S. Department of Energy, Office of Science, Basic Energy Sciences, under Award Number DE-SC0001090. Prof. Nathaniel C. Gilbert at CAMD kindly helped with the synchrotron X-ray diffraction analysis, and Dr. Dongmei Cao at the Louisiana State University Shared Instrument Facility provided the FE-SEM micrographs. Stephanie Beck of FPInnovations and Hee Jin Kim of the Southern Regional Research Center reviewed the manuscript. Acknowledgements are also made to Catrina Ford for technical assistance. Mention of trade names or commercial products in this publication is solely for the purpose of providing specific information and does not imply recommendation or endorsement by the U.S. Department of Agriculture. USDA is an equal opportunity provider and employer.

References

Agarwal UP, Ralph SA (1997) FT-Raman spectroscopy of wood: Identifying contributions of lignin and carbohydrate polymers in the spectrum of black spruce (*Picea mariana*). Appl Spectrosc 51:1648–1655. doi: 10.1366/0003702971939316

Agarwal UP (2014) 1064 nm FT-Raman spectroscopy for investigations of plant cell walls and other biomass materials. Front Plant Sci 5: 490

Agarwal UP, Ralph SA, Reiner RS, Baez C (2016) Probing crystallinity of never-dried wood cellulose with Raman spectroscopy. Cellulose 23:125–144. doi: 10.1007/s10570-015-0788-7

Ahvenainen P, Kontro I, Svedström (2016) Comparison of sample crystallinity determination methods by X-ray diffraction for challenging cellulose I materials. Cellulose 23:1073–1086

Atalla RH, Gast JC, Sindorf, DW, Bartuska VJ, Maciel GE (1980) Carbon-13 NMR spectra of cellulose polymorphs. J Am Chem Soc 102(9): 3249–3251

Atalla RH, Vanderhart DL (1984) Native cellulose: A composite of two distinctive crystalline forms. Science 223: 283–285

Barnette AL, Bradley LC, Veres BD, Schreiner EP, Park J, Park S, Kim SH (2011) Selective detection of crystalline cellulose in plant cell walls with sum frequency generation (SFG) vibration spectroscopy. Biomacromolecules 12:2434–2439

Barnette AL, Lee C, Bradley LC, Schreiner EP, Park H, Shin H, Cosgrove DJ, Park S, Kim SH (2012) Quantification of crystalline cellulose in lignocellulosic biomass using sum frequency generation (SFG) vibration spectroscopy and comparison with other analytical methods" Carbohydr Polym 89:802–809

Bertran MS, Dale BE (1986) Determination of cellulose accessibility by differential scanning calorimetry. J Appl Polym Sci 32:4241–4253

Brunauer S, Emmett PH, Teller E (1938) Adsorption of gases in multimolecular layers. J Am Chem Soc 60:309–319

Chen L, Wang Q, Hirth K, Baez C, Agarwal UP,Zhu JY (2015) Tailoring the yield and characteristics of wood cellulose nanocrystals (CNC) using concentrated acid hydrolysis. Cellulose 22:1753–1762

Dollase WA (1986) Correction of intensities for preferred orientation in powder diffractometry: application of the March model. J Appl Crystallogr 19(4):267–272.

Driemeier C, Calligaris GA (2011) Theoretical and experimental developments for accurate determination of crystallinity of cellulose I materials. J Appl Cryst 44:184–192

Driemeier C (2014) Two-dimensional Rietveld analysis of celluloses from higher plants. Cellulose 21:1065–1073

Driemeier C, Francisco LH (2014) X-ray diffraction from faulted cellulose I constructed with mixed Iα–Iβ stacking. Cellulose 21:3161–3169

Duchemin B (2017) Size, shape, orientation and crystallinity of cellulose Iβ by X-ray powder diffraction using a free spreadsheet program. Cellulose 24:2727–2741

Forziati FH, Stone WK, Rowen JW, Appel WD (1950) Cotton powder for infrared transmission measurements. J Res Nat Bur Stand 45: 109–113

Foston MB, Hubbell CA, Ragauskas AJ (2011) Cellulose Isolation Methodology for NMR Analysis of Cellulose Ultrastructure. Materials 4:1985–2002

French AD (2014) Idealized powder diffraction patterns for cellulose polymorphs. Cellulose 21:885–896. DOI: 10.1007/s10570-013-0030-4

French AD, Santiago Cintrón M (2013) Cellulose polymorphy, crystallite size, and the Segal crystallinity index. Cellulose 20:583–588

French AD, Pérez S, Bulone V, Rosenau T, Gray D (2018) Cellulose, in Encyclopedia of Polymer Science and Technology DOI: 10.1002/0471440264.pst042.pub2

French AD, Kim HJ (2018) Cotton fiber structure, in Fang D ed. Cotton fiber, physics and biology DOI: 10.1007/978-3-030-00871-0_2

Harris DM, Corbin K, Wang T, Gutierrez R, Bertolo AL, Petti C, Smilgies D-M, Estevez JM, Bonetta D, Urbanowicz BR, Ehrhardt DW, Somerville CR, Rose JKC, Hong M, Debolt S (2012) Cellulose microfibril crystallinity is reduced by mutating C-terminal transmembrane region residues CESA1^{A903V} and CESA3^{T942I} of cellulose synthase. Proc Natl Acad Sci 109:4098–4103

Hearle JWS (1958) A fringed fibril theory of structure in crystalline polymers. J Polym Sci 28:432–435

Holzwarth U, Gibson N (2011) The Scherrer equation versus the'Debye-Scherrer equation'. Nat Nanotechnol 6:534

Howell C, Hastrup ACS, Jara R, Larsen FH, Goodell B, Jellison J (2011) Effects of hot water extraction and fungal decay on wood crystalline cellulose structure. Cellulose 18:1179–1190

Huang S, Makarem M, Kiemle SN, Hamedi H, Sau M, Cosgrove DJ, Kim SH (2018a) Inhomogeneity of cellulose microfibril assembly in plant cell walls revealed with sum frequency generation microscopy. J Phys Chem B 122:5006–5019

Huang S, Makarem M, Kiemle SN, Zheng Y, Xin H, Ye D, Gomez EW, Gomez ED, Cosgrove DJ, Kim SH (2018b) Investigating dehydration-induced physical strains of cellulose microfibrils in plant cell walls. Carbohydr Polym 197:337–348

Ilharco LM, Garcia AR, Silva JL, Ferreira FV (1997) Infrared Approach to the S tudy of Adsorption on Cellulose: Influence of Cellulose Crystallinity on the Adsorption of Benzophenone. Langmuir 13(15): 4126-4132.

Isogai A, Atalla RH (1991) Amorphous celluloses stable in aqueous media: Regeneration from SO2–amine solvent systems. J Polym Sci Part A Polym Chem 29:113–119

Kirui A, Ling Z, Kang X, Dickwella Widanage MC, Mentink—Vigier F, French AD, Wang T (2019) Atomic resolution of cotton cellulose structure enabled by

Dynamic Nuclear Polarization Solid-State NMR. Cellulose 26:XXXX–XXYY

Klug HP, Alexander LE (1974) X-ray diffraction procedures: for polycrystalline and amorphous materials. X-Ray Diffr Proced Polycryst Amorph Mater 2nd Ed. Klug HP, Alexander LE Eds., pp 992 ISBN 0-471-49369-4 Wiley-VCH

Kono H, Numata Y (2006) Structural investigation of cellulose I α and I β by 2D RFDR NMR spectroscopy: determination of sequence of magnetically inequivalent D-glucose units along cellulose chain. Cellulose 13:317–326

Langan P, Nishiyama Y, Chanzy H (2001) X-ray structure of mercerized cellulose II at 1 Å resolution. Biomacromolecules 2:410–416

Larsson PT, Hult EL, Wickholm K, Pettersson E, Iversen T (1999) CP/MAS ^{13}C NMR spectroscopy applied to structure and interaction studies on cellulose I. Solid State Nucl Magn Reson 15:31-40

Lee CM, Mohamed NMA, Watts HD, Kubicki JD, Kim SH (2013) Sum-frequency-generation vibration spectroscopy and density functional theory calculations with dispersion corrections (DFT-D2) for cellulose Iα and Iβ. J Phys Chem B 117:6681–6692

Lee C, Kafle K, Park Y-B, Kim SH (2014) Probing crystal structure and mesoscale assembly of cellulose microfibrils in plant cell walls, tunicate tests, and bacterial films using vibrational sum frequency generation (SFG) spectroscopy" Phys Chem Chem Phys 16:10844–10853

Lee CM, Kafle K, Huang S, Kim SH (2015a) Multimodal broadband vibrational sum frequency generation (MM-BB-V-SFG) spectrometer and microscope. J Phys Chem B 120:102–116

Lee CM, Kubicki JD, Xin B, Zhong L, Jarvis MC, Kim SH (2015b) Hydrogen bonding network and OH stretch vibration of cellulose: Comparison of computational modeling with polarized IR and SFG spectra. J Phys Chem B 119:15138–15149

Lee CM, Chen X, Weiss PA, Jensen L, Kim SH (2016a) Quantum mechanical calculations of vibrational sum-frequency-generation (SFG) spectra of cellulose: dependence of the ch and oh peak intensity on the polarity of cellulose chains within the SFG coherence domain. J Phys Chem Lett 8:55–60

Lee CM, Dazen K, Kafle K, Moore A, Johnson DK, Park S, Kim SH (2016b) Correlations of apparent cellulose crystallinity characterized by estimated from different characterization techniques: XRD, NMR, IR, Raman, & and SFG. Adv Polym Sci 271:115–131

Liu Y, Thibodeaux D, Gamble G, Bauer P, VanDerveer D (2012) Comparative investigation of Fourier transform infrared (FT-IR) spectroscopy and X-ray diffraction (XRD) in the determination of cotton fiber crystallinity. Appl Spectrosc 66:983–986

Liu Y, Kim HJ (2015) Use of attenuated total reflection fourier transform infrared (ATR FT-IR) Spectroscopy in direct, nondestructive, and rapid assessment of developmental cotton fibers grown in planta and in culture. Appl Spectrosc 69:1004–1010

Lutterotti L, Bortolotti M, Ischia G, Lonardelli I, Wenk H-R, (2007) Rietveld texture analysis from diffraction images, Z Kristallogr, Suppl. 26, 125–130

Makarem M, Lee CM, Sawada D, O'Neill HM, Kim SH (2017) Distinguishing surface versus bulk hydroxyl groups of cellulose nanocrystals using vibrational sum frequency generation spectroscopy. J Phys Chem Letts 9:70–75

Makarem M, Lee CM, Kafle K, Huang S, Chae I, Yang H, Kubicki JD, Kim SH (2019) Probing cellulose structures with vibrational spectroscopy. Cellulose 26:XXXX-XXYY

Massiot D, Fayon F, Capron M, King I, Le Calvé S, Alonso B, Durand J-O, Bujoli B, Gan Z, Hoatson G (2002) Modelling one- and two- dimensional solid-state NMR spectra. Magn Reson Chem 40:70–76

Millett MA, Effland MJ, Caulfield DF (1979) Influence of fine grinding on the hydrolysis of cellulosic materials-acid vs. enzymatic. Adv Chem Ser 181:71–89

Nelson ML, O’Connor RT (1964a) Relation of certain infrared bands to cellulose crystallinity and crystal lattice type. Part II. A new infrared ratio for estimation of crystallinity in celluloses I and II. J Appl Polym Sci 8:1325–1341. doi: 10.1002/app.1964.070080323

Nelson ML, O’Connor RT (1964b) Relation of certain infrared bands to cellulose crystallinity and crystal latticed type. Part I. Spectra of lattice types I, II, III and of amorphous cellulose. J Appl Polym Sci 8:1311–1324

Newman RH, Hemmingson JA (1990) Determination of the degree of cellulose crystallinity in wood by carbon-13 Nuclear Magnetic Resonance Spectroscopy. Holzforschung 44:351–356

Newman RH, Hill SJ, Harris PJ (2013) Wide-angle X-ray scattering and solid-state nuclear magnetic resonance data combined to test models for cellulose microfibrils in mung bean cell walls. Am Soc Plant Biol 163:1558–1567

Nishiyama Y, Langan P, Chanzy H (2002) Crystal structure and hydrogen-bonding system in cellulose Iβ from synchrotron X-ray and neutron fiber diffraction. J Am Chem Soc 124:9074–9082

Nishiyama Y, Sugiyama J, Chanzy H, Langan P (2003a) Crystal structure and hydrogen bonding system in cellulose Iα from synchrotron x-ray and neutron fiber diffraction. J Am Chem Soc 125:14300–14306. doi: ja0257319

Nishiyama Y, Kim U-J, Kim D-Y, Katsumata KS, May RP, and Langan P (2003b) Periodic disorder along ramie cellulose microfibrils. Biomacromolecules 4:1013–1017

Oh SY, Yoo D, Shin Y, Kim HC, Kim HY et al (2005) Crystalline structure analysis of cellulose treated with sodium hydroxide and carbon dioxide by means of X-ray diffraction and FTIR spectroscopy. Carbohyd. Res. 340: 2376-2391.

Park S, Baker JO, Himmel ME, Parrilla PA, Johnson DK (2010) Cellulose crystallinity index: measurement techniques and their impact on interpreting cellulase performance. Biotechnol Biofuels 3:10

Park YB, Lee CM, Koo B-W, Park S, Cosgrove DJ, Kim SH (2013) Monitoring meso-scale ordering of cellulose in intact plant cell walls using sum frequency generation (SFG) spectroscopy. Plant Physiol 163:907–913

Phyo P, Wang T, Yang Y, O’Neill H, Hong M (2018) Direct determination of hydroxymethyl conformations of plant cell wall cellulose using ^{1}H polarization transfer solid-state NMR. Biomacromolecules 19:1485–1497

Popa NC, Balzar D (2008) Size-broadening anisotropy in whole powder pattern fitting. J Appl Cryst 41:615–627

Application to zinc oxide and interpretation of the apparent crystallites in terms of physical models

Reyes DCA, Skoglund N, Svedberg A, Eliasson B, Sundman O (2016) The influence of different parameters on the mercerisation of cellulose for viscose production. Cellulose 23:1061–1072

Rietveld H (1969) A profile refinement method for nuclear and magnetic structures. J Appl Crystallogr 2:65–71

Rodriguez-Navarro AB (2006) XRD2DScan: new software for polycrystalline materials characterization using two-dimensional X-ray diffraction. J Appl Crystallogr 39:905–909

Röhrling J, Potthast A, Rosenau T, Lange T, Borgards A, Sixta H, Kosma P (2002) A novel method for the determination of carbonyl groups in cellulosics by fluorescence labeling. 2. Validation and applications. Biomacromolecules 3: 969–975

Rollin JA, Zhu Z, Sathitsuksanoh N, Zhang YP (2011) Increasing cellulose accessibility is more important than removing lignin: A comparison of cellulose solvent- based lignocellulose fractionation and soaking in aqueous ammonia. Biotechnol Bioeng 108:22–30

Sarko A, Nishimura H, Okano T (1987) Crystalline alkali-celllulose complexes as intermediates during mercerization. ACS Symp Ser 340:169–177

Schenzel K, Fischer S, Brendler E (2005) New method for determining the degree of cellulose I crystallinity by means of FT Raman spectroscopy. Cellulose 12:223–231. doi: 10.1007/s10570-004-3885-6

Schroeder LR, Gentile VM, Atalla RH (1986) Nondegradative preparation of amorphous cellulose. J Wood Chem Technol 6:1–14

Segal L, Creely JJ, Martin a. E, Conrad CM (1959) An empirical method for estimating the degree of crystallinity of native cellulose using the X-Ray diffractometer. Text Res J 29:786–794. doi: 10.1177/004051755902901003

Sehaqui H, Zhou Q, Berglund LA (2011) High-porosity aerogels of high specific surface area prepared from nanofibrillated cellulose (NFC). Compos Sci Technol 71:1593–1599

Shibazaki H, Kuga S, Okano T (1997) Mercerization and acid hydrolysis of bacterial cellulose. Cellulose 4:75–87

Sugiyama J, Persson J, Chanzy H (1991) Combined infrared and electron diffraction study of the polymorphism of native celluloses. Macromolecules 24:2461–2466

Takahashi H, Lee D, Dubois L, Bardet M, Hediger S, De Paëpe G (2012) Rapid natural- abundance 2D ^{13}C–^{13}C correlation spectroscopy using Dynamic Nuclear Polarization Enhanced Solid- State NMR and matrix- free sample preparation. Angew Chemie Int Ed 51:11766–11769

Thygesen A, Oddershede J, Lilholt H, Thomsen AB, Ståhl (2005) On the determination of crystallinity and cellulose content in plant fibres. Cellulose 12:563–576

Vanderfleet OM, Reid MS, Bras J, Heux L, Godoy-Vargas J, Panga MKR, Cranston ED (2019) Insight into thermal stability of cellulose nanocrystals from new hydrolysis methods with acid blends. Cellulose 26:XXX–XXX (This issue)

Viëtor RJ, Newman RH, Ha MA, Apperley DC, Jarvis MC (2002) Conformational features of crystal-surface cellulose from higher plants. Plant J 30(6) 721–731

Wang T, Hong M (2016) Solid-state NMR investigations of cellulose structure and interactions with matrix polysaccharides in plant primary cell walls. J Exp Bot 67: 503–514

Wertz J-L, Mercier JP, Bédué O (2010) Cellulose sciense and technology. Taylor& Francis Group

Wickholm K, Larsson PT, Iversen T (1998) Assignment of non-crystalline forms in cellulose I by CP/MAS ^{13}C NMR spectroscopy. Carbohydr Res 312:123–129

Wiley JH, Atalla RH (1987) Band assignments in the Raman spectra of celluloses. Carbohydr Res 160:113–129

Xiaohui J, Bowden M, Brown EE, Zhang X (2015) An improved X-ray diffraction method for cellulose crystallinity measurement. Carbohydr Polym 123:476–481

Yang H, Wang T, Oehme D, Petridis L, Hong M, Kubicki JD (2018) Structural factors affecting ^{13}C NMR chemical shifts of cellulose: a computational study. Cellulose 25:23–36

Young RA ed. (1993) The Rietveld Method. IUCr Monographs in Crystallography. 5. International Union of Crystallography, Oxford University Press, New York, NY. pp. 298